การเปลี่ยนสถานะเชิงโครงสร้างและสมบัติทางกายภาพภายใต้ความดันสูงของ

$CuIn_xGa_{1-x}Se_2$ที่ผ่านการโดป

นายประยูรศักดิ์ เปลื้องผล

วิทยานิพนธ์นี้เป็นส่วนหนึ่งของการศึกษาตามหลักสูตรปริญญาวิทยาศาสตรดุษฎีบัณฑิต

สาขาวิชาฟิสิกส์ ภาควิชาฟิสิกส์

คณะวิทยาศาสตร์ จุฬาลงกรณ์มหาวิทยาลัย

ปีการศึกษา 2554

ลิขสิทธิ์ของจุฬาลงกรณ์มหาวิทยาลัย

STRUCTURAL PHASE TRANSITIONS AND PHYSICAL PROPERTIES OF DOPED

$CuIn_xGa_{1-x}Se_2$ UNDER HIGH PRESSURE

Mr. Prayoonsak Pluengphon

A Dissertation Submitted in Partial Fulfillment of the Requirements

for the Degree of Doctor of Philosophy Program in Physics

Department of Physics

Faculty of Science

Chulalongkorn University

Academic Year 2011

Thesis Title   Structural Phase Transitions and Physical Properties of
                      Doped $CuIn_xGa_{1-x}Se_2$ under High Pressure
By   Mr. Prayoonsak Pluengphon
Field of Study   Physics
Thesis Advisor   Assistant Professor Thiti Bovornratanaraks, Ph. D.
Thesis Co-advisor   Sornthep Vannarat, Ph. D.

Accepted by the Faculty of Science, Chulalongkorn University in Partial
Fulfillment of the Requirements for the Doctoral Degree

……………………………………………….. Dean of the Faculty of Science

(Professor Supot Hannongbua, Dr. rer. nat.)

THESIS COMMITTEE

……………………………………………….. Chairman

(Assistant Professor Patcha Chatraporn, Ph. D.)

………………………………………………. Thesis Advisor

(Assistant Professor Thiti Bovornratanaraks, Ph. D.)

……………………………………………….. Thesis Co-advisor

(Sornthep Vannarat, Ph. D.)

……………………………………………….. Examiner

(Assistant Professor Somchai Kiatgamolchai, Ph. D.)

……………………………………………….. Examiner

(Chatchai Srinitiwarawong, Ph. D.)

……………………………………………….. External Examiner

(Associate Professor Yongyut Laosiritaworn, Ph. D.)

ประยูรศักดิ์ เปลื้องผล: การเปลี่ยนสถานะเชิงโครงสร้างและสมบัติทางกายภาพ ภายใต้ความดันสูงของ $CuIn_xGa_{1-x}Se_2$ ที่ผ่านการโดป (STRUCTURAL PHASE TRANSITIONS AND PHYSICAL PROPERTIES OF DOPED $CuIn_xGa_{1-x}Se_2$ UNDER HIGH PRESSURE) อ. ที่ปรึกษาวิทยานิพนธ์หลัก: ผศ.ดร.ธิติ บวรรัตนารักษ์, อ. ที่ปรึกษาวิทยานิพนธ์ร่วม: ดร.ศรเทพ วรรณรัตน์, 81 หน้า.

วิธี *Ab initio* ถูกใช้ในการคำนวณการเปลี่ยนสถานะเชิงโครงสร้างและสมบัติทางกายภาพภายใต้ความดันสูงของสารกึ่งตัวนำ ในขั้นต้นสารประกอบเชิงซ้อน เช่น $CuIn_xGa_{1-x}Se_2$ ได้ถูกศึกษา ภายใต้ความดันสูงสาร $CuInSe_2$ มีการเปลี่ยนโครงสร้างจาก $I\bar{4}2d \longrightarrow Fm\bar{3}m \longrightarrow Cmcm$ ที่ความดัน 12 และ 42 GPa ตามลำดับ ช่องว่างแถบพลังงานที่คำนวณด้วยฟังชันนอล sX-LDA ในโครงสร้าง $I\bar{4}2d$ เพิ่มขึ้นในอัตรา 39.6 meV/GPa ซึ่งสอดคล้องกับการทดลอง แต่ช่องว่างแถบพลังงานถูกปิดในโครงสร้าง $Fm\bar{3}m$ และ $Cmcm$ ดังนั้นเฟสโลหะได้รับการสมมติสำหรับโครงสร้างทั้งสอง วิถีของการเปลี่ยนเฟสจาก $Fm\bar{3}m$ ไปยัง $Cmcm$ ได้ถูกพิสูจน์ กำแพงศักย์ระหว่างสองโครงสร้างคือ 17 meV ซึ่งสมมูลกับพลังงานอุณหภูมิ 198 K สำหรับการศึกษาผลของโซเดียมบน $CuIn_{0.5}Ga_{0.5}Se_2$ ภายใต้ความดันสูงนั้น การเปลี่ยนเฟสของ $CuIn_{0.5}Ga_{0.5}Se_2$ เหมือนกับ $CuInSe_2$ ความเข้มข้นต่ออะตอมของโซเดียมถูกทดสอบที่ 0.1, 1.0 และ 6.25 เปอร์เซ็นต์ การเพิ่มขึ้นของพลังงานใน Na_{InGa} มีค่ามากกว่าใน Na_{Cu} ดังนั้นโซเดียมชอบการแทนที่บนตำแหน่งของคอปเปอร์มากกว่าบนแกลเลียมหรืออินเดียมซึ่งสอดคล้องกับงานวิจัยก่อนหน้า โซเดียมลดความแข็งของ $CuIn_{0.5}Ga_{0.5}Se_2$ ซึ่งสามารถเพิ่มโซเดียมที่ความดันสูงได้ง่ายกว่าที่ความดันปกติ ผลกระทบมีนัยสำคัญมากที่สุดที่ความเข้มข้น 6.25 เปอร์เซ็นต์ ค่าความหนาแน่นของสถานะที่บริเวณใกล้ๆขอบบนของแถบวาเลนซ์มีค่าเพิ่มขึ้นเนื่องจากผลของการเจือโซเดียมซึ่งนำไปสู่การเพิ่มขึ้นของความหนาแน่นของโฮล

ภาควิชา	ฟิสิกส์	ลายมือชื่อนิสิต _____
สาขาวิชา	ฟิสิกส์	ลายมือชื่อ อ.ที่ปรึกษาวิทยานิพนธ์หลัก _____
ปีการศึกษา	2554	ลายมือชื่อ อ.ที่ปรึกษาวิทยานิพนธ์ร่วม _____

5173830023 : MAJOR   PHYSICS

KEYWORDS : DFT / DOPED SEMICONDUCTOR / HIGH PRESSURE / PHASE TRANSITION / QUATERNARY COMPOUND

PRAYOONSAK PLUENGPHON: STRUCTURAL PHASE TRANSITIONS AND PHYSICAL PROPERTIES OF DOPED CuIn$_x$Ga$_{1-x}$Se$_2$ UNDER HIGH PRESSURE. ADVISOR: ASST. PROF. THITI BOVORNRATANARAKS, Ph. D., CO-ADVISOR: SORNTHEP VANNARAT, Ph. D., 81 pp.

Ab initio method was used to calculate the structural phase transitions and physical properties of semiconductors. At the beginning, the complex compounds which have been widely used in solar cell industry such as CuIn$_x$Ga$_{1-x}$Se$_2$ were studied. For high pressure phases and electronic properties of CuInSe$_2$, it was found that the CIS transform in the following way; $I\bar{4}2d \longrightarrow Fm\bar{3}m \longrightarrow Cmcm$ at 12 GPa and 42 GPa respectively. The sX-LDA band gap in the $I\bar{4}2d$ structure increases at the rate of 39.6 meV/GPa, in fair agreement with 30 meV/GPa obtained from the photoabsorption experiment. The band gap is closed in the $Fm\bar{3}m$ and $Cmcm$ structures. Therefore, the metallic phase has been assumed for both structures. The path of transformation from $Fm\bar{3}m$ to $Cmcm$ was derived. The barrier between these two phases was estimated. The upper bound of the potential barrier is 17 meV which is equivalent to thermal energy at 198 K. For studying the effects of Na on high pressure phases of CuIn$_{0.5}$Ga$_{0.5}$Se$_2$, it was found that the high pressure phase transitions of CuIn$_{0.5}$Ga$_{0.5}$Se$_2$ appear to be remarkable similar to that of the CuInSe$_2$ phase transitions. The Na concentrations were chosen at 0.1, 1.0 and 6.25 %. The positive mixing energy of Na$_{InGa}$ is higher than that of Na$_{Cu}$. Thus, Na substitutes on Cu sites are more energetically favorable than on Ga or In sites which is in good agreement with the previous reports. The Na substitutes reduce the hardness of CIGS and they can be easily added into the CuIn$_{0.5}$Ga$_{0.5}$Se$_2$ under high pressure comparing to the addition under ambient pressure. The most significant effects occur at Na concentration of 6.25%. It was found that the EDOS near the VBM is increased noticeably in the chalcopyrite phase. This should lead to the increase of the hole density.

Department : _____Physics_____ Student's Signature _____

Field of Study : _____Physics_____ Advisor's Signature _____

Academic Year : _____2011_____ Co-advisor's Signature _____

Acknowledgements

Contents

List of Tables

List of Figures

CHAPTER I
Introduction

Energy crisis is one of the most important problems for mankind in this century and solar cell is a practical choice of clean energy for solving this problem. In the past, solar cell is an unpopular energy source, as shown in Figure 1.1 (a), due to low efficiency of the photovoltaic process. However, it becomes a practical choice because of an unlimited source of sunlight. Solar cell is a device that converts the energy of sunlight directly into electricity using photovoltaic effect. It consists of multilayer of both n and p type semiconductors, as shown in Figure 1.1 (b), such as Silicon, Gallium Arsenide, Indium Phosphide, Cadmium Telluride and Copper Indium Diselenide. The electrical and optical properties of solar cell highly depend on the type of semiconducting materials. The absorption coefficient for some semiconductors may be increased by the external factors such as temperature, pressure and impurities. The effect of fabrication process on the improvement solar-material was widely investigated by the experimental scientist. Several fabrication techniques have been developed in the past decade based on experimental trial and error approach. Recently, theoretical studies have been widely used for materials simulation. It has become more important matter to understand the physics behind the fabrication process which is largely governed by the two important thermodynamic variables, pressure and temperature. Most of theoretical solution for material properties was carried out using the first-principle study (*ab initio*). This technique relies on fundamental laws of nature without additional assumptions or special models. The advantage of *ab initio* study is that it can be carried out without knowing any experimental data of the system. Nowadays, the accurate simulations of materials are drastically increased by the advance of theoretical and computational techniques accompanied by the rapidly growing of computing power. The basic laws in physics and quantum chemistry are widely adopted in several programs for *ab initio* simulation. Moreover, the novel information obtained from this sophisticated theoretical approach has widened our understanding in nature and properties of materials.

The Role of Renewable Energy in the Nation's Energy Supply, 2008

Total = 99.305 Quadrillion Btu

Total = 7.301 Quadrillion Btu

Petroleum 37%

Natural Gas 24%

Coal 23%

Renewable Energy 7%

Nuclear Electric Power 9%

Solar 1%
Geothermal 5%
Wind 7%
Hydropower 34%
Biomass 53%

(a)

Ni/Al contacts

ZnO:Al + ZnO:i

n-type CdS

p-type CuInGaSe$_2$

Mo

Glass
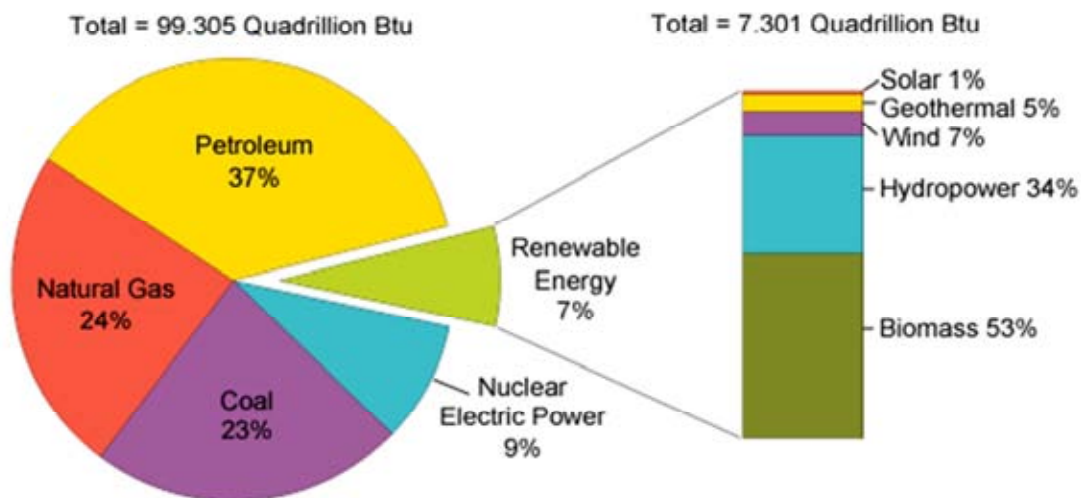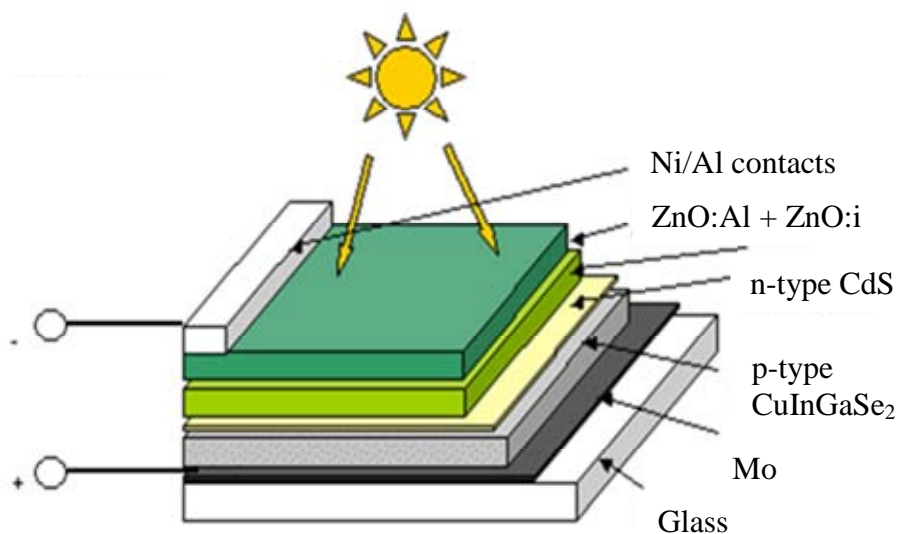
(b)

Figure 1.1: (a) U.S. energy consumption statistics in 2008. Only 7% of U.S. energy supply came from renewable energy in 2008 and out of that only 1% is solar energy (http://www.simply-solarpower.com/photovoltaic-cell.html). (b) The structure of CuInGaSe$_2$ solar cell (http://www.energy-daily.com).
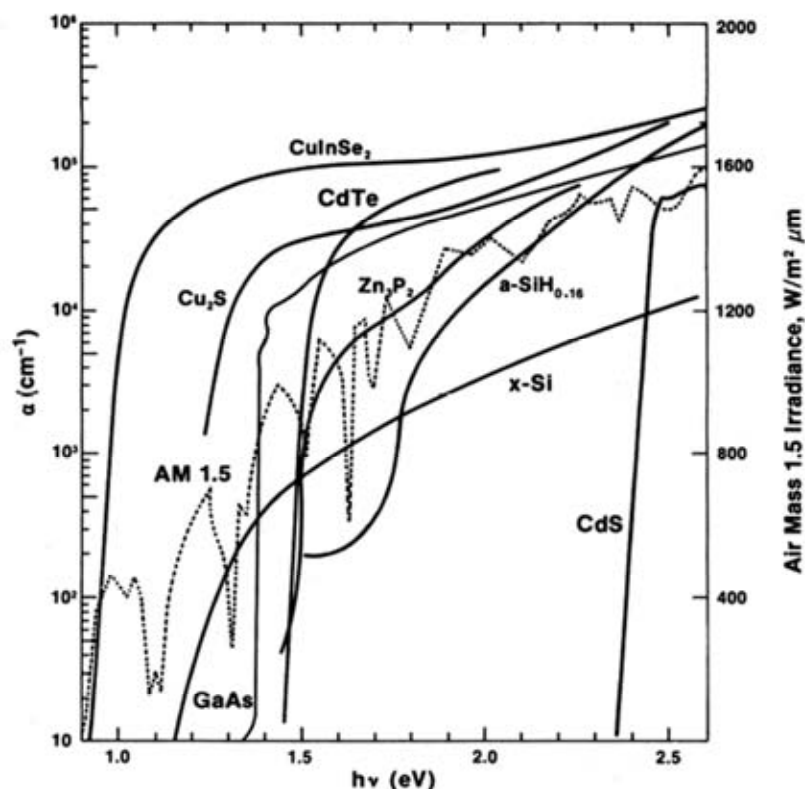
Figure 1.2: Comparisons the absorption spectrum of CuInSe$_2$ and other photovoltaic semiconductors [1].

In previous studies, the Copper Indium Diselenide (CIS) has recently emerged as a very promising material for photovoltaic solar-energy application, due partially to the fact that it is the strong absorbing semiconductor under sunlight, shown in Figure 1.2. CIS is also widely used in optical industries. The high pressure phases of CIS were studied using diamond anvil cells and x-ray diffraction experiments [2, 3]. In 1996, the crystal structure and phase transitions under high pressure of CIS were investigated by T. Tinoco *et al*. [2]. They studied the crystal structure of CIS under the maximum pressure of 29.0 GPa by using energy dispersive x-rays diffraction with synchrotron radiation and diamond anvil cell. It is well known that the ambient pressure phase of CIS is the chalcopyrite phase ($I\bar{4}2d$), as shown in Figure 1.3(a). The first phase transitions have been observed at 7.6 GPa and the high-pressure phases have been indexed as a cubic structure ($Fm\bar{3}m$), as shown in Figure 1.3(b). The volume reduction at the phase transition is about 11 %.
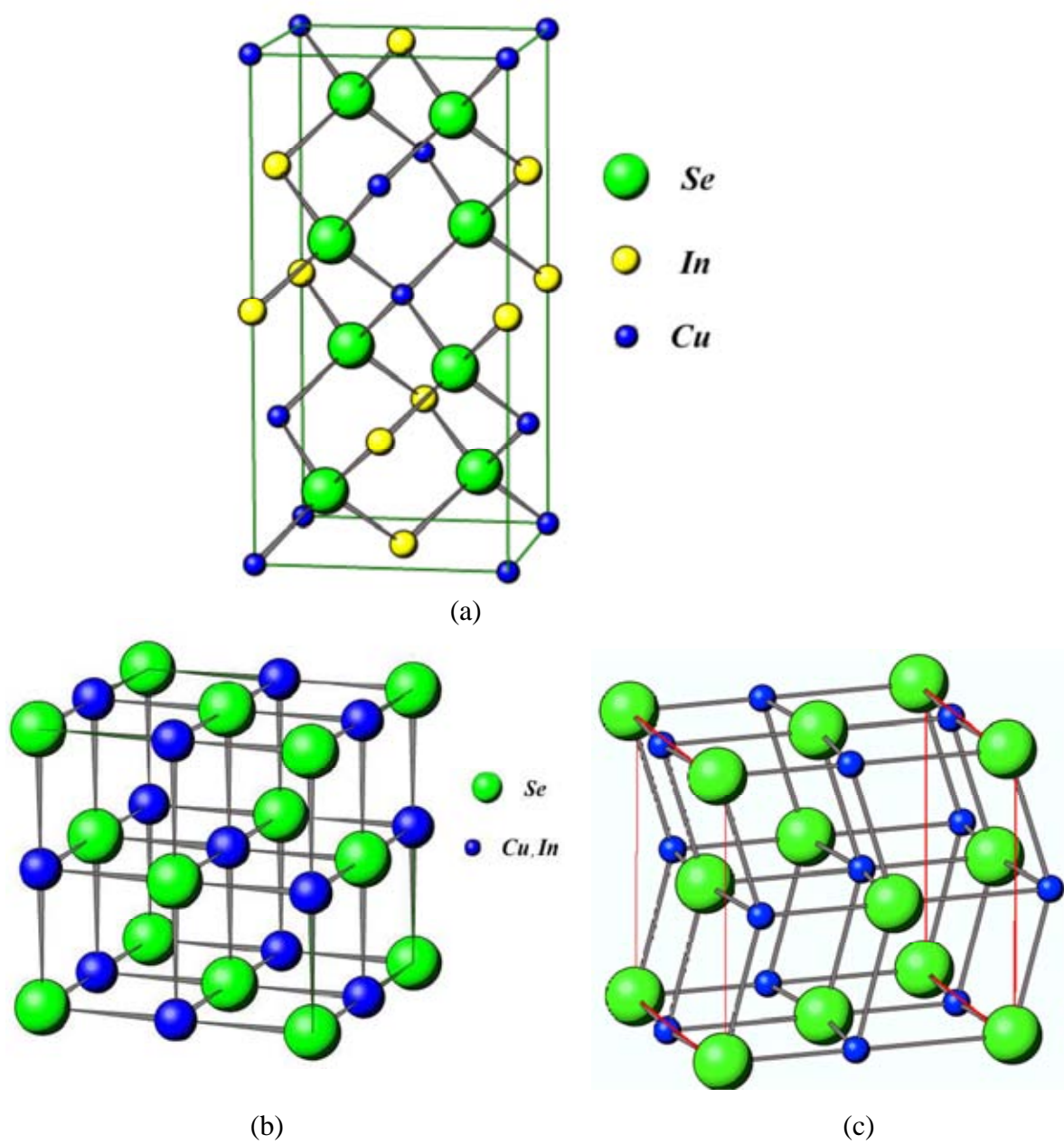
Figure 1.3: The high pressure phases of CIS [9] (a) the upper structure is chalcopyrite phase ($I\bar{4}2d$) (b) the left handed side structure is NaCl-like cubic phase ($Fm\bar{3}m$) and (c) the right handed side structure is the orthorhombic (*Cmcm*) phase.

More recently, T. Bovornratanaraks *et al.* [3] extended the study of CIS up to 53.2 GPa. They observed an orthorhombic (*Cmcm*) structure, as shown in Figure 1.3(c), at 33.9 GPa, and the $Fm\bar{3}m$ is completely transformed to *Cmcm* at 43.9 GPa. Apart from the structural phase transitions, the CIS band gap and optical properties under pressure were studied in the $I\bar{4}2d$ phase [4-8]. Gonźalez *et al*. [4] studied the optical absorption of monocrystalline CIS samples grown by Bridgman technique and chemical vapor transport method. At 300 K, they found that the energy gap increases linearly with pressure between 0 – 7 GPa at the rate of 30 meV/GPa. It was proposed that the band gap increase comes from I-VI bond reduction as a result of *pd* bonding of the valence orbitals under pressure [1].
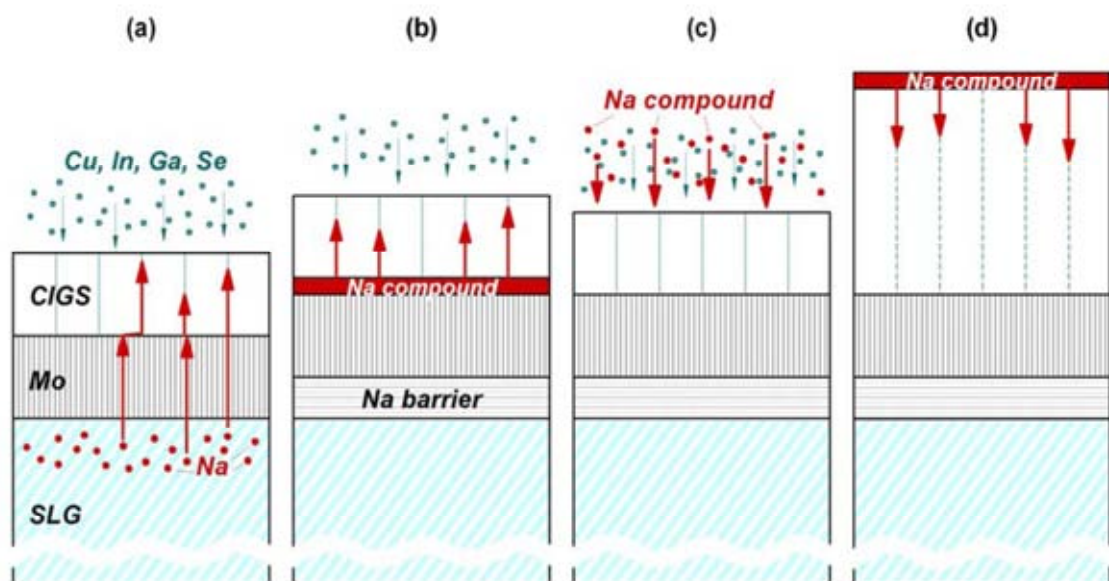
Figure 1.4: The experimental processes of Na doping into CIGS. (a) Na is diffused from the substrate into CIGS during growth. (b) Na is supplied by a thin Na-containing precursor layer deposited prior to CIGS growth. (c) A Na compound is co-evaporated during the CIGS-deposition process. (d) Na is diffused into as-grown absorbers using a post-deposition treatment [9].

By studying $CuInSe_2$, $CuGaSe_2$ and $CuAlSe_2$, Maeda and Wada [7] concluded that *sp* bonding of the III-VI bond dominate the conduction band and a shorter bond length results in a wider band gap. Vidal *et al*. [8] studied the electronic properties of CIS by using any functional such as local density approximation (LDA), Green's function methods with GW approximation [8], Heyd-Scuseria-Ernzerhof (HSE06) hybrid functional and etc. They found that the band gap in the chalcopyrite phase depends strongly on the lattice displacement. The trend of the GW band gap was compared with the LDA results. Despite of underestimating the band gap values, the LDA results exhibit a similar trend to the GW results.

The achievement of maximum cell efficiencies could be obtained by adding a small amount of Sodium (Na) into Copper Indium Gallium Diselenide (CIGS) [9–19]. The simplest method to incorporate Na is to diffuse from soda-lime glass substrates through the Mo back contact into the growing CIGS layer [13, 14]. Another method is that Na can be supplied by a thin Na containing precursor layer deposited prior to CIGS growth, diffused into as-grown absorbers using a post-deposition treatment, and co-evaporated during the CIGS-deposition process [15–19], as shown in Figure 1.4. For the ternary semiconductors such as chalcopyrite I-III-VI_2 compounds, the Na atoms can substitute any of the two metal sites of group-I or III, and the types of carriers would depend on the site of Na on chalcopyrite [17]. Wei *et al.* [18] suggested that Na impurities have three effects on $CuInSe_2$ (CIS). First, Na replaces on Cu site, and the compound $NaInSe_2$ has a larger band gap and positive mixing enthalpy. Second, the effect of Na on the surface of CIS is to dissociate O_2 into atomic oxygen, and substitutes into Se-site vacancies, and it increases the hole density. Third, Na becomes a defect at the Cu or In site. They found that Na on the Cu site has no effect on the electronic levels in the band gap, whereas Na on the In site produces some acceptor levels. Other reported effects were the increase of the hole density, conductivity, and grain sizes, and the suppression of the formation of the ordered defect compound. Li *et al.* [19] studied Na-doped CIS by first-principle calculations. They used a super cell method and replaced a Na atom on one of the Cu sites (Na_{Cu}). They observed that 6.25% Na_{Cu} increases the CIS band gap by 0.114 eV at ambient pressure. Another effect of 6.25% Na_{Cu} is to increase the density of states near valence band maximum (VBM). They found that 6.25% Na_{Cu} has stronger effect on the hole density of CIS than 8.33% and 12.5% Na. From previous studies, Na has

significant effects on physical properties of CIS. Na becomes a point defect at the Cu or In site. The impurities of Na were widely studied at ambient pressure. These previous works are the motivation for studying structural phase transitions and physical properties of doped semiconductors under high pressure.

In this work, the experimental phase transitions under pressure of CIS will be verified by *ab initio* calculation, as will be shown in Chapter III. The work has been carried out and extended to find the transitions pressure of $CuIn_xGa_{1-x}Se_2$ where x = 0, 0.5 and 1. The *ab initio* method is based on density functional theory (DFT) which treat the electron density as a basic variable. All ground state properties are determined by the ground state density. The total energy of many-body system is a unique functional of electron density. The minimum total energy of a system is related to the ground state electron density. The bulk properties of materials will be determined from basic laws in the 1^{st}Brillouin zone. In DFT model, Kohn-Sham equations will be solved by self-consistent field method. The results of calculation depend on types of exchange correlation functional in Kohn-Sham equations. The calculations will be done by using the self-consistent field (SCF) method. The generalized-gradient approximation (GGA) functional of Perdew-Burke-Ernzerhof (PBE) will be adopted for the exchange-correlation energy in the calculations. For phase transitions, the stability of high-pressure phases will be investigated from the slopes of energy-volume curves and the enthalpy, H = E + PV. The procedure is based on optimizing the structure at fixed volumes and using the 3rd order Birch-Murnaghan equation of state (EOS). From equation of state, it can be used to extract thermodynamics properties of bulk semiconductor by partial differentiations. For studying at extremely high pressure (in GPa), the pressure range of semiconducting region in CIGS will be evaluated. The physical properties will also be investigated under the extreme conditions. The calculation results will be compared with previous experimental reports. The electronic properties such as band structure, electronic density of states (EDOSs) were also presented. For DFT band structure calculation, it is well known that the LDA and GGA functionals neglect the effect of excited states; as a result, some properties such as energy gap will be underestimated comparing to those obtained from experimental studies. The standard Kohn-Sham orbitals (GGA or LDA) were obtained from the Kohn-Sham equations which exploited only the local potentials. However, the non-local potential can be added into the Kohn-Sham

equations by using the screen-exchange local density approximation (sX-LDA) functional. In this work, the DFT band gap of CIGS was investigated using sX-LDA functional. In Chapter IV, the effects of Na on $CuIn_{0.5}Ga_{0.5}Se_2$ at ambient pressure were analyzed up to the high pressure phases. Na impurity was added into $CuIn_{0.5}Ga_{0.5}Se_2$ by using virtual crystal approximation and super cell methods. The efficiency of adding Na into CIGS under high pressure was described from the mixing energy. From incorporation of Na into the CIGS, it is expected that the properties of CIGS such as bulk modulus, electronic density of states and hole density will highly depend on doping concentration. The novel information about the impurity Na into CIGS under high pressure will also be discussed in the Chapter IV and V.

CHAPTER II
Theoretical Background

In quantum mechanics, Schrödinger's equation and Werner Heisenberg's matrix mechanics share a major success in explaining a single particle in any given potential. The evolution with time was described by the time-dependent Schrödinger equation. The solutions are commonly used to evaluate the energy levels and other properties of a single electron. However, this technique is not practical for the systems that contain large number of electrons which is called many-body system. In such problem, the quantum theory for a system of ions and interacting electrons is based on solving a many-body Schrödinger equation in the form

$$\hat{H}\psi = E\psi, \tag{2.1}$$

where $\hat{H}$ is the Hamiltonian of the system,

$$\hat{H} = -\sum_{i} \frac{\hbar^2}{2m} \nabla_i^2 - \sum_{i,I} \frac{Z_I e^2}{|\mathbf{r}_i - \mathbf{R}_I|} + \frac{1}{2} \sum_{\substack{i,j \\ (j \neq i)}} \frac{e^2}{|\mathbf{r}_i - \mathbf{r}_j|}$$
$$- \sum_{I} \frac{\hbar^2}{2M} \nabla_I^2 + \frac{1}{2} \sum_{\substack{I,J \\ (J \neq I)}} \frac{Z_I Z_J e^2}{|\mathbf{R}_I - \mathbf{R}_J|}. \tag{2.2}$$

The right handed side terms of Eq. 2.2 consist of the kinetic energy of electrons, electron-ion interactions, electron-electron interactions, kinetic energy of ions and ion-ion interactions respectively. This equation is the central equation of condensed matter which contains all properties of many-body system. However, we cannot exactly solve for the solutions of this equation. By using basic approximations, we can assume that the ions is moving slowly in space and the electrons is instantaneously responding to the ionic motion, so ψ has an explicit dependence on only electrons motion. This is called "Born-Oppenheimer approximation" [20]. From Born-Oppenheimer approximation, we can explicitly separate the solid wave function into the product of electron and ion wave functions. The ion-ion effect can be omitted and the electron part will play an important role in this problem. The ion-ion

interactions term in Eq. 2.2 can be set to be a constant, which can be added from observable properties related to the nuclei. Therefore, Hamiltonian of the electronic system for the ions at rest becomes

$$\hat{H} = -\sum_i \frac{\hbar^2}{2m} \nabla_i^2 - \sum_{i,I} \frac{Z_I e^2}{|\mathbf{r}_i - \mathbf{R}_I|} + \frac{1}{2} \sum_{\substack{i,j \\ (j \neq i)}} \frac{e^2}{|\mathbf{r}_i - \mathbf{r}_j|}. \tag{2.3}$$

This Hamiltonian cannot exactly be solved by using the eigenvalue problem in Eq. 2.1 due to the complex nature of many-electron wave functions. The first approximation of many-electron wave functions was introduced by Hartee's theory [21]. It was suggested that the complicated many-electron wave function can be reduced to the product of single-electron wave functions. However, this idea fails to explain the antisymmetric property of the electron wave functions. Later, Hartree and Fock (HF) [21-22] suggested that the many-electron wave function was proposed as a Slater determinant of the single-electron wave functions. The Hartree-Fock theory can be applied to tiny systems. It includes the antisymmetric property of the electron wave functions and exchange interaction but it still excludes the correlation effects. In addition, HF method is not suitable for the systems which possess large number of electrons because of its high consumption in computing memory. For a solid system, the density functional theory (DFT) is a more suitable approach for the reason that DFT contained exchange-correlation interactions which has taken the simulation close to a real system. In the following section, the DFT will be discussed in great detail.

2.1 Density Functional Theory

Density functional theory (DFT) is one of the most popular and successful technique to solve many-body problems. In principle, DFT is an exact method started from the basic laws but the practical process used some approximations for exchange-correlation functional. The first principle studying of DFT started from Hohenberg-Kohn theorems [23].

2.1.1 Hohenberg-Kohn theorems

Hohenberg-Kohn theorems for the systems of a non-degenerate ground state consist of two theorems as follow:

The first theorem: For the system of interacting particles in an external potential, $V_{ext}(\mathbf{r})$, there exists a one to one correspondence between the external potential and ground state density ($n_0(\mathbf{r})$). Consequently, the ground state expectation value of any observable quality A is a unique functional of the electron density, i.e.

$$A = A[n(\mathbf{r})] \text{ and } \left\langle \psi \left| \hat{A} \right| \psi \right\rangle = A[n_0(\mathbf{r})] \tag{2.4}$$

The second theorem: For a given external potential applied to an interacting particles system, we can determine the ground state energy by minimizing total energy with respect to density by using the variational principle. The exact ground state energy, E_0, corresponding to the correct ground state density, $n_0(\mathbf{r})$, is given by

$$E_0 = E[n_0(\mathbf{r})] \leq E[n(\mathbf{r})] \tag{2.5}$$

2.1.2 The definition of functional

The function is a rule of mapping a variable x to a scalar $g(x)$. While *functional* ($F[g]$) is the mapping of a function, $g(x)$, to the value of the function $F[g]$ [24-26]. The $F[g]$ may be viewed as a function of a large collection of variables. In the same way, $g(x)$, we can think of a vector $\mathbf{r}$ as a set of value r_i in $g(\mathbf{r})$. We can think of $g(x)$ as the indexed set of values g_i. The functional derivative of $F[g]$, denoted $\dfrac{\delta F}{\delta g(x)}$, is the path of difference for all test function , $f(x)$, in the form

$$\left\langle \frac{\delta F[g(x)]}{\delta g(x)}, f(x) \right\rangle = \int \frac{\delta F[g(x)]}{\delta g(x')} f(x')dx'$$
$$= \lim_{\varepsilon \to 0} \frac{F[g(x)+\varepsilon f(x)] - F[g(x)]}{\varepsilon}$$
$$= \frac{d}{d\varepsilon} F[g(x)+\varepsilon f(x)] \Big|_{\varepsilon=0} \tag{2.6}$$

In physics, it is common to use Dirac delta function, $\delta(x-x')$, as a test function.

$$\frac{\delta F[g(x)]}{\delta g(x')} = \lim_{\varepsilon \to 0} \frac{F[g(x) + \varepsilon \delta(x - x')] - F[g(x)]}{\varepsilon} \tag{2.7}$$

By using Eq. 2.6, when we have the functional $E_{xc}[n(\mathbf{r})] = \int g_{xc}(\mathbf{r}, n(\mathbf{r})) d\mathbf{r}$, then

$$\left\langle \frac{\delta E_{xc}[n]}{\delta n}, f \right\rangle = \lim_{\varepsilon \to 0} \frac{E_{xc}[n + \varepsilon f] - E_{xc}[n]}{\varepsilon}$$

$$= \lim_{\varepsilon \to 0} \frac{\int [g_{xc}(n(\mathbf{r}) + \varepsilon f) - g_{xc}(n(\mathbf{r}))] d\mathbf{r}}{\varepsilon}$$

$$= \lim_{\varepsilon \to 0} \frac{\int [[g_{xc}(n(\mathbf{r})) + \varepsilon f \frac{\partial g_{xc}(n(\mathbf{r}))}{\partial n} + ...] - g_{xc}(n(\mathbf{r}))] d\mathbf{r}}{\varepsilon}$$

$$= \lim_{\varepsilon \to 0} \frac{\int \varepsilon f \frac{\partial g_{xc}(n(\mathbf{r}))}{\partial n} d\mathbf{r}}{\varepsilon} \text{ (to the first order approximation)}$$

$$= \int \frac{\partial g_{xc}(n(\mathbf{r}))}{\partial n} f d\mathbf{r}$$

$$= \left\langle \frac{\partial g_{xc}(n(\mathbf{r}))}{\partial n}, f \right\rangle$$

We then have the result as

$$\frac{\delta E_{xc}}{\delta n(\mathbf{r})} = g'_{xc}(n(\mathbf{r})). \tag{2.8}$$

Alternatively, the $g_{xc}(n(\mathbf{r}))$ can be expanded to the multi-variable parameter q_i in the other form such as $g_{xc}(n(\mathbf{r})) = \sum_i g_{xc}(q_i)$. The partial derivatives of $g_{xc}(n(\mathbf{r}))$ are

$$\frac{\partial g_{xc}}{\partial q_i} = g'_{xc}(q_i). \tag{2.9}$$

Next, we will emphasize on the derivation of a complex variable (z) and its conjugate (z^*). For example, we have a real function $f(z, z^*)$ or $f(z_r, z_i)$, where real part $z_r = (z + z^*)/2$ and imaginary part $z_i = (z - z^*)/2i$. The two partial derivatives of f with respect to z and z^* will be real because n is always real. The partial derivatives of f with respect to z^* is

$$\frac{\partial f}{\partial z^*}\bigg|_z = \frac{\partial f}{\partial z_r}\bigg|_{z_i} \frac{\partial z_r}{\partial z^*}\bigg|_z + \frac{\partial f}{\partial z_i}\bigg|_{z_r} \frac{\partial z_i}{\partial z^*}\bigg|_z$$

$$= \frac{1}{2}\left(\frac{\partial f}{\partial z_r}\bigg|_{z_i} + i\frac{\partial f}{\partial z_i}\bigg|_{z_r}\right). \tag{2.10}$$

The real and imaginary components give both derivatives simultaneously. When we minimize over all possible values, we need only one condition

$$\frac{\partial f}{\partial z^*}\bigg|_z = 0. \tag{2.11}$$

2.1.3 Kohn-Sham equations

According to the Hohenberg-Kohn theorems, all observable qualities are functionals of electrons density. The numerical determination of the ground state density in DFT was evaluated by Kohn and Sham [27]. They proposed that Kohn-Sham equation is a Schrödinger-like equation as a functional of density. This equation obtained from the Hohenberg-Kohn energy functional ($E[n]$) which can be written as

$$E[n] = T_s[n] + U[n] + E_{xc}[n] \tag{2.12}$$

where T_s is the non-interacting kinetic energy of electrons, U is the potential energy including the electron-electron interaction (Hartree energy) and external potential energy due to a coulomb potential of nuclei, and E_{xc} is the exchange-correlation energy due to the interaction of the electrons. The potential from nuclei on the single electron at position (**r**) is

$$V_{nu} = \sum_I \frac{Z_I e^2}{|\mathbf{r} - \mathbf{R}_I|} \tag{2.13}$$

If the number of electrons in volume dV is $n(\mathbf{r})dV$, we have the total potential energy of the electrons interacting with the nuclei is

$$U_{nu-el} = \int V_{nu}(\mathbf{r})n(\mathbf{r})d\mathbf{r}. \tag{2.14}$$

For electron-electron interaction, the total coulomb potential for single electron at point $\mathbf{r}$ from another electron at $\mathbf{r}'$ can be written as

$$\phi(\mathbf{r}) = e^2 \int \frac{n(\mathbf{r}')d\mathbf{r}'}{|\mathbf{r}-\mathbf{r}'|}.$$ (2.15)

From the electrostatics this integral is equivalent to the Poisson's equation in the form

$$\nabla^2 \phi(\mathbf{r}) = -4\pi e^2 n(\mathbf{r})$$ (2.16)

And then, the total interaction of electrons with themselves is

$$U_{el-el} = \frac{1}{2} \int \phi(\mathbf{r})n(\mathbf{r})d\mathbf{r}.$$ (2.17)

The electron density and kinetic energy can be obtained from the orbitals. Because the square of each orbital gives the distribution of the electrons in that orbital, the total electron density can be written in form

$$n(\mathbf{r}) = \sum_i^{occ} f_i |\psi_i(\mathbf{r})|^2,$$ (2.18)

where f_i the number of electrons in each orbital ψ_i, usually there are 2 electrons. The total kinetic energy can be obtained from the sum over all kinetic energy of electrons in each orbital in the form

$$T_{el} = \sum_i f_i \int \psi_i^*(\mathbf{r}) \left(-\frac{\hbar^2}{2m} \nabla^2 \psi_i(\mathbf{r}) \right) dV.$$ (2.19)

In advanced quantum mechanics, the electron density in Eq. 2.18 is only the average density, but the actual density is fluctuated. The total energy is corrected by adding the approximation of exchange-correlation correction, in which one of the simplest function is

$$E_{xc} = \int g_{xc}(n(\mathbf{r}))d\mathbf{r}.$$ (2.20)

The total energy in Eq. 2.12 can be written as

$$E[\{\psi_i(\mathbf{r})\}] = \sum_i f_i \int \psi_i^*(\mathbf{r})\left(-\frac{\hbar^2}{2m}\nabla^2\psi_i(\mathbf{r})\right)d\mathbf{r} + \int V_{nu}(\mathbf{r})n(\mathbf{r})d\mathbf{r}$$

$$+\frac{1}{2}\int \phi(\mathbf{r})n(\mathbf{r})d\mathbf{r} + \int g_{xc}(n(\mathbf{r}))d\mathbf{r}. \tag{2.21}$$

The total energy in Eq. 2.21 is functional of $n(\mathbf{r})$ or $\{\psi_i(\mathbf{r})\}$. By using variational method [25-30], we take the derivatives of real functions. We need to include the normality constraint of each orbital with a separate Lagrange multiplier (λ_i). The condition of minimization is

$$\frac{\delta}{\delta\psi_i^*(\mathbf{r})}\left(T_{el}+U_{nu-el}+U_{el-el}+E_{xc}+U_{nu-nu}-\sum_i\lambda_i\int\psi_i^*(\mathbf{r})\,\psi_i(\mathbf{r})dV\right)=0. \tag{2.22}$$

By using the same technique in Eq. 2.8, the kinetic energy functional has one $\psi_i^*(\mathbf{r})$ term and then we get

$$\frac{\delta T_{el}}{\delta\psi_i^*(\mathbf{r})} = \frac{\delta}{\delta\psi_i^*(\mathbf{r})}\left(\sum_i f_i\int\psi_i^*(\mathbf{r})\left(-\frac{\hbar^2}{2m}\nabla^2\psi_i(\mathbf{r})\right)dV\right)$$

$$=\frac{\partial}{\partial\psi_i^*(\mathbf{r})}\left(f_i\psi_i^*(\mathbf{r})\left(-\frac{\hbar^2}{2m}\nabla_i^2\psi_i(\mathbf{r})\right)\right)\Bigg|_{\psi_i(\mathbf{r})}$$

$$=-\frac{\hbar^2}{2m}f_i\nabla_i^2\psi_i(\mathbf{r}). \tag{2.23}$$

For the functional derivative in U_{nu-el} term, $V_{nu}(\mathbf{r})$ is unchanged with the variation of $\psi_i^*(\mathbf{r})$, it can be written as

$$\frac{\delta U_{nu-el}}{\delta\psi_i^*(\mathbf{r})} = \frac{\delta}{\delta\psi_i^*(\mathbf{r})}\left(\int V_{nu}(\mathbf{r})n(\mathbf{r})dV\right)$$

$$=\frac{\partial V_{nu}(\mathbf{r})n(\mathbf{r})}{\partial\psi_i^*(\mathbf{r})} = V_{nu}(\mathbf{r})\frac{\partial\left(\sum_i^{occ} f_i\left|\psi_i(\mathbf{r})\right|^2\right)}{\partial\psi_i^*(\mathbf{r})}\Bigg|_{\psi_i(\mathbf{r})}$$

$$\frac{\delta U_{nu-el}}{\delta \psi_i^*(\mathbf{r})} = V_{nu}(\mathbf{r}) f_i \psi_i(\mathbf{r}). \tag{2.24}$$

In the term of electron-electron energy, the potential function and density change with $\psi_i^*(\mathbf{r})$. We used the Poisson's equation in 2.16 to get

$$\int (\delta\phi) n dV = \int (\delta\phi) \frac{\nabla^2 \phi(\mathbf{r})}{-4\pi e^2} dV = \int \phi \nabla^2 \left(\frac{\delta\phi(\mathbf{r})}{-4\pi e^2} \right) dV = \int \phi(\delta n) dV,$$

where we have moved the $\nabla^2 \phi(\mathbf{r})$ to $\nabla^2 \delta\phi(\mathbf{r})$ by integrating by parts twice. We can find the functional derivative in U_{el-el} from $\int \phi(\delta n) dV$ as

$$\frac{\delta U_{el-el}}{\delta \psi_i^*(\mathbf{r})} = \frac{\delta \frac{1}{2} \int \phi(\mathbf{r}) n(\mathbf{r}) dV}{\delta \psi_i^*(\mathbf{r})} = \phi(\mathbf{r}) \left. \frac{\delta n(\mathbf{r})}{\delta \psi_i^*(\mathbf{r})} \right|_{\psi_i(\mathbf{r})} = f_i \phi(\mathbf{r}) \psi_i(\mathbf{r}). \tag{2.25}$$

For exchange-correlation term, it was derived in Eq. 2.8. We have

$$\frac{\delta E_{xc}}{\delta \psi_i^*(\mathbf{r})} = \frac{\partial g_{xc}(n(\mathbf{r}))}{\partial n(\mathbf{r})} \frac{\partial n(\mathbf{r})}{\partial \psi_i^*(\mathbf{r})} = f_i g_{xc}'(n(\mathbf{r})) \psi_i(\mathbf{r}). \tag{2.26}$$

For the potential U_{nu-nu}, the functional derivative is zero because it is not changed with $\psi_i^*(\mathbf{r})$. Finally, we obtain

$$\frac{\delta}{\delta \psi_i^*(\mathbf{r})} \left(-\sum_i \lambda_i \int \psi_i^*(\mathbf{r}) \psi_i(\mathbf{r}) dV \right) = -\lambda_i \psi_i(\mathbf{r}). \tag{2.27}$$

From minimizing the Eq. 2.22, the Kohn-Sham equations can be obtained as

$$\hat{H}_{iKS} \psi_i = \left[-\frac{\hbar^2}{2m} \nabla_i^2 + V_{eff} \right] \psi_i = \frac{\lambda_i}{f_i} \psi_i = \varepsilon_i \psi_i, \tag{2.28}$$

where $\frac{\lambda_i}{f_i} = \varepsilon_i$ and the effective potential (V_{eff}) is given by

$$V_{eff} = \int \frac{n(\mathbf{r}')e^2}{|\mathbf{r}-\mathbf{r}'|} d^3\mathbf{r} - \sum_I \frac{Z_I e^2}{|\mathbf{r}-\mathbf{R}_I|} + \frac{\delta E_{xc}[n(\mathbf{r})]}{\delta n(\mathbf{r})}. \tag{2.29}$$

The first, second and third terms are the Hartree potential ($V_H(\mathbf{r})$), the external potential ($V_{ext}(\mathbf{r})$) and the exchange-correlation potential ($V_{xc}(\mathbf{r})$) respectively. The Kohn-Sham equation is the *like* Schrödinger's equation, but it is not Schrödinger's equation because we can span the electron density on any arbitrary basis function, shown as Eq. 2.18. Moreover, the Kohn-Sham orbitals (ψ_i) is not an exact wave function for explaining the properties of one electron in the system. But the ground state density can be obtained from the summation of overall occupied one-electron states, shown in Eq. 2.18. The difficult problem for solving Eq. 2.28 is that we cannot exactly evaluate the exchange-correlation term in Eq. 2.29. However, it can be solved by using some novel approximation as follows.
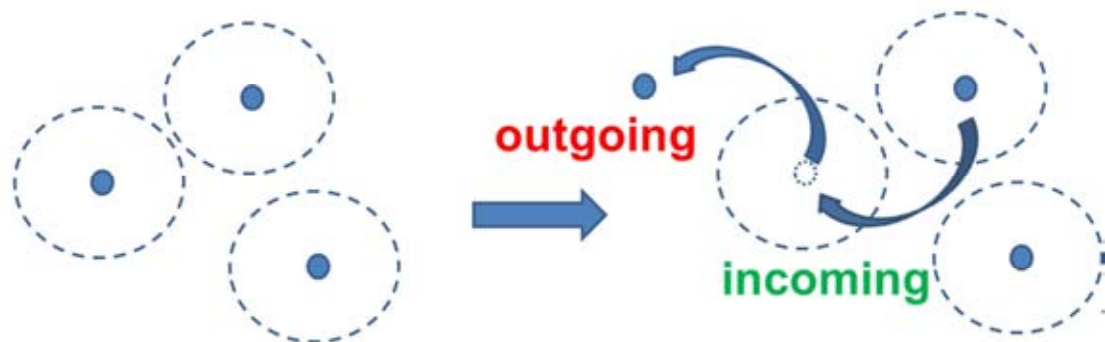
Figure 2.1: A model that can be used to explain the correlation effect in many-body system. The transition states of electrons are the correlated motions.

2.1.4 Exchange-correlation approximations

The exchange-correlation term consists of the exchange and correlation effects in the many-electron system. The exchange effect contains the antisymmetric of electronic wave function in HF method. But the correlation effect is obtained from the correlated motions of electrons in a system, shown in Figure 2.1. For Kohn-Sham solution, we use Kohn-Sham orbitals, which is not the antisymmetric wave function. Therefore, the exchange and correlation effects need to be included in the exchange-correlation approximations. The conventional and well known approximations for exchange-correlation function are Local Density Approximation (LDA) and Generalized Gradient Approximation (GGA) [29-32].

The Local Density Approximation or LDA is the simplest method for the exchange-correlation approximations in Kohn-Sham equations. It assumes that the exchange-correlation energy per electron is the known exchange-correlation energy per electron of a homogeneous electron gas with the same density at any position $\mathbf{r}$. The approximate functional E_{xc} can be written as

$$E_{xc}\left[n\left(\mathbf{r}\right)\right]=\int\varepsilon_{xc}\left(n\left(\mathbf{r}\right)\right)n\left(\mathbf{r}\right)d^{3}r \qquad (2.30)$$

and

$$\frac{\delta E_{xc}\left[n\left(\mathbf{r}\right)\right]}{\delta n(\mathbf{r})}=\frac{\partial\left(n\left(\mathbf{r}\right)\varepsilon_{xc}\left(n\left(\mathbf{r}\right)\right)\right)}{\partial n(\mathbf{r})}, \qquad (2.31)$$

with

$$\varepsilon_{xc}\left(n\left(\mathbf{r}\right)\right)\equiv\varepsilon_{homo}\left[n\left(\mathbf{r}\right)\right]. \qquad (2.32)$$

The $\varepsilon_{xc}\left(n\left(\mathbf{r}\right)\right)$ is not a functional, but it is a function of $n\left(\mathbf{r}\right)$ at a particular point of space. The expressions for ε_{xc} based on various methods. The LDA is widely used in the slowly varying density systems. However, the LDA scheme is not well described in many cases such as the rapidly varying density systems. There are many attempts to improve the LDA by including higher-order terms of electron density such as the gradient of density which is called Generalized Gradient Approximation (GGA). The Eq. 2.30 can be rewritten as

$$E_{xc}\left[n\left(\mathbf{r}\right)\right]=\int\varepsilon_{xc}\left(n\left(\mathbf{r}\right),\nabla n\left(\mathbf{r}\right)\right)n\left(\mathbf{r}\right)d^{3}r \qquad (2.33)$$

Recently, the GGA functional has been developed as Perdew-Wang (PW), Perdew-Wang 91 (PW91) and Perdew-Burke-Ernzerhof (PBE) respectively [29-32]. The modern functional GGA-PBE [30-32] was adopted in the calculation of semiconducting systems reported in this work. However, LDA and GGA give the wrong band gap for semiconductors. Because the Kohn-Sham orbitals obtained from the models of exchange-correlation functional in Eq. 2.30 and 2.33 are not enough to explain splitting band gap between valence and conduction band in semiconductor. In this work, the band gap calculation method was improved by using the screen-exchange local density approximation (sX-LDA) [33-36]. The sX-LDA is a combination of LDA and Hartree-Fock theory. The intrinsic local screen-exchange interaction has been replaced by a non-local interaction and a generalized Kohn-Sham

equation. In the local potential (using the functional in Eq. 2.30 or 2.33), the standard Kohn-Sham orbitals are the lowest eigenvalue solutions of an equation in the form

$$\left[-\frac{\hbar^2}{2m}\nabla_i^2 + \mu^{loc}(\mathbf{r}) \right]\psi_i = E\psi_i. \tag{2.34}$$

By using sX-LDA functional, the local potential ($\mu^{loc}(\mathbf{r})$) can be modified by adding a *non-local* integral operator $V^{NL}(\mathbf{r},\mathbf{r}')$. The Kohn-Sham equations with sX-LDA becomes

$$\left[-\frac{\hbar^2}{2m}\nabla_i^2 + \mu^{loc}(\mathbf{r}) + \int V_{xc}^{NL}(\mathbf{r},\mathbf{r}')\psi_i(\mathbf{r}')d\mathbf{r}' \right]\psi_i(\mathbf{r}) = E\psi_i(\mathbf{r}). \tag{2.35}$$

$V_{xc}^{NL}(\mathbf{r},\mathbf{r}')$ is a *direct functional* of the orbitals. We begin with the original definition of the exchange energy, U_x, in term of the Kohn-Sham orbitals as

$$U_x = -\frac{1}{2}\sum_{ikjq}d\mathbf{r}d\mathbf{r}'\frac{\phi_{ik}^*(\mathbf{r})\phi_{ik}^*(\mathbf{r}')\phi_{jq}(\mathbf{r})\phi_{jq}(\mathbf{r}')}{|\mathbf{r}-\mathbf{r}'|}, \tag{2.36}$$

where j and $\mathbf{q}$ label bands and $\mathbf{k}$-points in the same way that i and $\mathbf{k}$ do. This is used to calculate the exchange energy in HF method. sX-LDA attempts to incorporate some of the effects of correlation into Eq. 2.36. One of the effects of correlation is to effectively screen the effect of exchange at long range. This can be achieved in a simple manner by multiplying the integrand of exchange energy by a factor that decays exponentially with increasing electron-electron separation in the form

$$E_{xc}^{NL} = -\frac{1}{2}\sum_{ikjq}d\mathbf{r}d\mathbf{r}'\frac{\phi_{ik}^*(\mathbf{r})\phi_{ik}^*(\mathbf{r}')\phi_{jq}(\mathbf{r})\phi_{jq}(\mathbf{r}')}{|\mathbf{r}-\mathbf{r}'|}e^{-k_s|\mathbf{r}-\mathbf{r}'|}, \tag{2.37}$$

where k_s is the reciprocal screening length. From non-local exchange-correlation energy, E_{xc}^{NL}, in Eq. 2.37, the non-local potential $V_{xc}^{NL}(\mathbf{r},\mathbf{r}')$ is given by

$$V_{xc}^{NL}(\mathbf{r},\mathbf{r}') = -\frac{1}{2}\sum_{jq}\frac{\phi_{jq}(\mathbf{r})\phi_{jq}(\mathbf{r}')}{|\mathbf{r}-\mathbf{r}'|}e^{-k_s|\mathbf{r}-\mathbf{r}'|}. \tag{2.38}$$

In this work, the sX-LDA method has been tested and it indicates that this functional provide more reliable approach for solving band-gap problem in semiconductor materials. However, the calculation using sX-LDA functional requires a significantly increasing in computing time comparing to the usual LDA and GGA.

2.1.5 The secular equation

The method for solving Kohn-Sham equations is described as follows. First, the Kohn-Sham orbitals can be expanded as a linear combination of an arbitrary basis function, $\varphi_i(\mathbf{r})$, as

$$\psi_n(\mathbf{r}) = \sum_{i=1}^{Q} c_{in} \varphi_i(\mathbf{r}), \tag{2.39}$$

where c_{in} are the sets of coefficients and Q is the number of basis function. Next, the Kohn-Sham orbitals in Eq. 2.39 are substituted in Kohn-Sham equations, multiplying with the complex conjugate of the basis function, $\varphi_j(\mathbf{r})$, and then integrating in real space to obtain

$$\sum_{i=1}^{Q} c_{in} \int \varphi_j^*(\mathbf{r}) \hat{H}_{iKS} \varphi_i(\mathbf{r}) d\mathbf{r} = \sum_{i=1}^{Q} c_{in} \varepsilon_i \int \varphi_j^*(\mathbf{r}) \varphi_i(\mathbf{r}) d\mathbf{r}, \tag{2.40}$$

This equation is denoted by the Hamiltonian matrix ($\mathbf{H}$), coefficient matrix ($\mathbf{C}$), eigenvalue matrix ($\boldsymbol{\varepsilon}$) and overlap matrix ($\mathbf{O}$) in the matrix form as $\mathbf{HC} = \boldsymbol{\varepsilon}\mathbf{OC}$, which is called "secular equation". $\mathbf{H}$ and $\mathbf{O}$ are the $Q \times Q$ matrices [37-39]. The secular equation can be solved by the numerical simulation.

2.1.6 Periodic potential system

For the periodic potential system in solids, we can consider the complex system by using Bloch theorem [40, 41]. The electron wave function of periodic crystal is the product of plane waves and periodic function $u_{nk}(\mathbf{r})$ as

$$\psi_{n\mathbf{k}}\left(\mathbf{r}\right)=u_{n\mathbf{k}}\left(\mathbf{r}\right)e^{i\mathbf{k}\cdot\mathbf{r}}, \tag{2.41}$$

where $\mathbf{k}$ is a wave vector and n is a band index. Under Bloch theorem, the eigenvalue and wave function must relate with the conditions

$$E(\mathbf{k})=E(\mathbf{k}+\mathbf{G}) \tag{2.42}$$

and

$$\psi_{n\mathbf{k}}\left(\mathbf{r}\right)=\psi_{n(\mathbf{k}+\mathbf{G})}\left(\mathbf{r}\right). \tag{2.43}$$

$\mathbf{G}$ is the reciprocal lattice vector. The maximum value of $\mathbf{G}$ ($\mathbf{G}_{max}$) relates to the cutoff energy

$$E_{cut}=\frac{\hbar^2\mathbf{G}^2_{max}}{2m}. \tag{2.44}$$

We define the periodic function as a summation of the plane wave basis sets, and the wave function can be written as

$$\psi_{n\mathbf{k}}\left(\mathbf{r}\right)=\sum_{j}c_{nj}\left(\mathbf{k}\right)e^{i(\mathbf{k}+\mathbf{G})\cdot\mathbf{r}}. \tag{2.45}$$

By inserting this wave function into Kohn-Sham equations and using the same method to get the Eq. 2.40, we obtain

$$\sum_{j'}\mathcal{H}_{j,j'}C_{nj'}\left(\mathbf{k}\right)=\varepsilon_n\left(\mathbf{k}\right)C_{nj}\left(\mathbf{k}\right), \tag{2.46}$$

where

$$\mathcal{H}_{j,j'}=\frac{\hbar^2}{2m}\left|\mathbf{k}+\mathbf{G}_j\right|^2\delta_{j,j'}+V_{eff}\left(\mathbf{G}_j-\mathbf{G}_{j'}\right) \tag{2.47}$$

and

$$V_{eff}\left(\mathbf{G}_j-\mathbf{G}_{j'}\right)=\int e^{-i\mathbf{G}_{j'}\cdot\mathbf{r}}V_{eff}\left(\mathbf{r}\right)e^{-i\mathbf{G}_j\cdot\mathbf{r}}d\mathbf{r}. \tag{2.48}$$

Eq. 2.46 is the secular equation in reciprocal lattice. We can get eigenvalues and eigenstates (Kohn-Sham orbitals) by diagonalization Eq. 2.47. Eq. 2.48 shows the transformation of the effective potential between the real and reciprocal spaces [37-39]. Therefore, the Kohn-Sham equations will be solved by using the secular equation and Fourier transform also [42]. It could be noticed that the eigenvalues and

eigenstates of Kohn-Sham equations have no physical meaning, but we can obtain the physical meaning from these results.

```
┌─────────────────────────────────┐
│   Pick a trial density n(r)     │
└─────────────────────────────────┘
                 ↓
┌─────────────────────────────────┐
│  Calculate V_H(n) and V_xc(n)   │ ◄──────────┐
└─────────────────────────────────┘            │
                 ↓                              │
┌─────────────────────────────────────────┐    │
│  Solve KS equation Ĥ_iKS ψ_i =          │    │
│  [ -ℏ²/2m ∇²_i + V_eff ] ψ_i = E ψ_i    │    │
│  by diagonalization of matrixes          │    │
└─────────────────────────────────────────┘    │
                 ↓                              │
┌─────────────────────────────────┐            │
│   Calculate new density n(r)    │            │
└─────────────────────────────────┘            │
                 ↓                              │
┌─────────────────────────────────┐            │
│   Is solution self-consistent?  │            │
└─────────────────────────────────┘            │
    │Yes              No│                       │
    ↓                   ↓                       │
┌─────────────┐  ┌──────────────────────────┐  │
│Compute total│  │ Generate new density n(r)│──┘
│   energy    │  │ (It is weighted from the │
└─────────────┘  │ current and previous     │
                 │ densities.)              │
                 └──────────────────────────┘
```
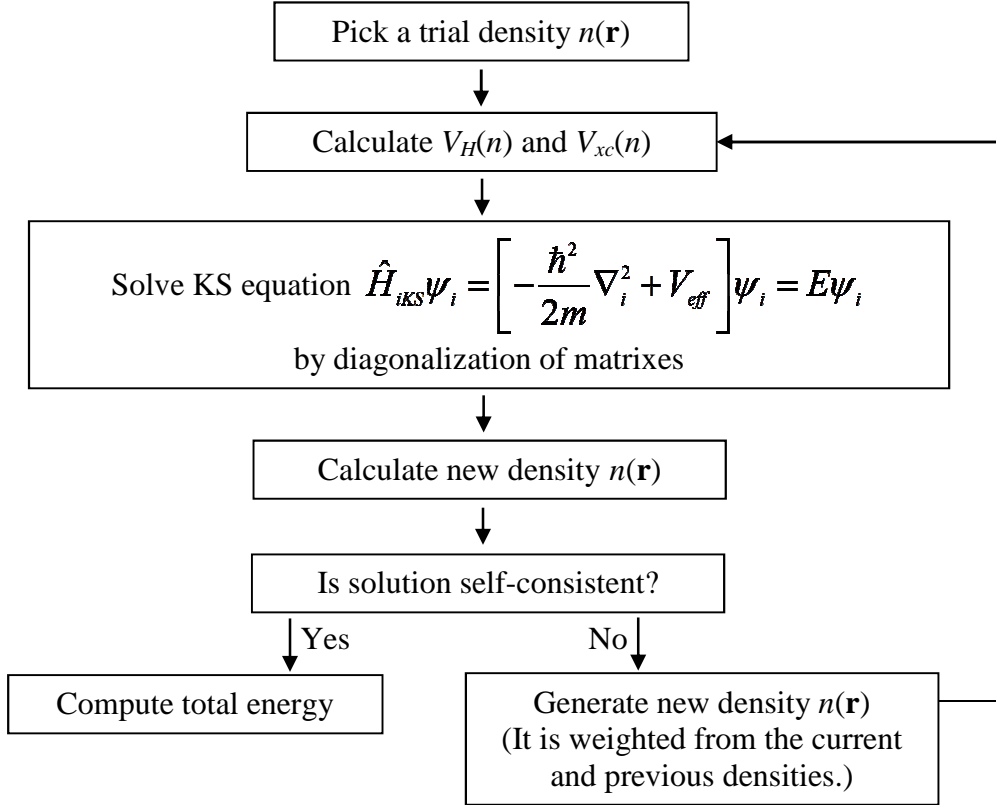
Figure 2.2: Flow chart of the computational procedure for the total energy calculation [42].

The physical meanings from Kohn-Sham equations are the true ground state density and the ground state total energy. The ground state total energy of a system (E_{tot}) can be written as

$$E_{tot} = \sum_i^{occ} \varepsilon_i - V_H[n] + E_{xc}[n] - \int \frac{\delta E_{xc}[n]}{\delta n} n(\mathbf{r}) d\mathbf{r}. \tag{2.49}$$

The algorithm for solving self-consistent Kohn-Sham equations is described in Figure 2.2. First, the pseudopotential of core ions is constructed from a given atomic numbers and positions of ions. The cutoff plane wave and k-point sampling are defined by input parameters. The electrons density is initially guessed by using a set of random coefficient of the plane waves basis set. The effective potential is then calculated from the guessed density. Next, Kohn-Sham equation is solved to get the total energies and Kohn-Sham orbitals. If the solution does not converge, the new density can be obtained from weighting of the current and previous densities and it is used as the initial density for next step. This process runs until the density is convergence. Finally, the output observable qualities can be calculated from the converged ground state density.

2.1.7 Cutoff energy and k-point sampling

The number of basis set ($\mathbf{G}_j$) is defined by the cutoff energy. The infinite value of $\mathbf{G}$ gives the exact Kohn-Sham solution as the infinite basis set. However, we cannot do that due to the limitation of calculation. The suitable cutoff energy for a system has to be estimated. The electronic states are defined only at a set of discrete $\mathbf{k}$ points. The number of k points is proportional to the volume of primitive cell in solid. The number of Kohn-Sham orbitals depends on the size of k-point sampling. It makes sense to divide the first Brillouin zone because it is invariant under Bloch's theorem. By using the Monkhorst-Pack method [43], we can write the integrated function $f(\mathbf{r})$ over the first Brillouin zone as

$$f(\mathbf{r}) = \frac{V}{8\pi^3} \int_{BZ} F(\mathbf{k}) d\mathbf{k} = \sum_j w_j F(\mathbf{k}_j), \qquad (2.50)$$

where $F(\mathbf{k})$ is the Fourier transform of $f(\mathbf{r})$, V is the cell volume and w_j are weighting factors. The k-points are distributed uniformly in space as $\mathbf{k}_j = x_{1j}\mathbf{b}_1 + x_{2j}\mathbf{b}_2 + x_{3j}\mathbf{b}_3$, where $\mathbf{b_i}$ are reciprocal lattice vectors. The infinite k-point sampling gives the exact solution. In the first step of all calculation, the optimum cutoff energy and k-point sampling must be tested for a system. The suitable k-point

depends on lattice constant. In DFT, we cannot know the exact solution, but we can find the error of converged solution by comparison with the higher cutoff and k-point. The electron density, total energy and other quantities can be obtained from the summation of the occupied states **k** in the first Brillouin zone.

2.1.8 Band structure calculation

From the solution of Kohn-Sham equations, we obtain the true ground state density, the Kohn-Sham obitals, the correct effective potential (in Figure 2.3) and hence the complete Hamiltonian. From Bloch theorem, the energy level can always be confined to the primitive unit cell of the reciprocal lattice or 1st Brillouin zone. The band index appears for each **k** resulting in many solutions, i.e.

$$\left\langle \psi_{nk} | \hat{H}_{KS} | \psi_{nk} \right\rangle = E_{nk}. \tag{2.51}$$

This equation leads to a description of the energy levels of electrons in a periodic potential in terms of a family of continuous functions E_{nk} which is the band structure of the solid.

$n(\mathbf{r})$ $\Longrightarrow$ $V(\mathbf{r})$
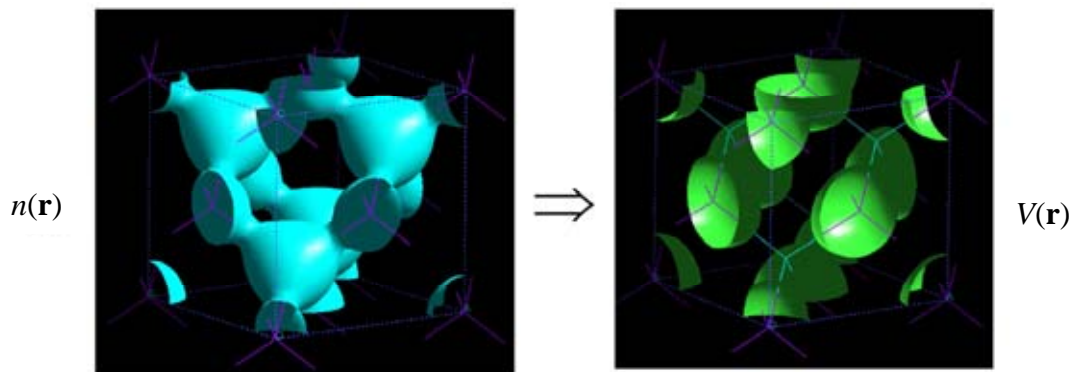
Figure 2.3: The equi-surface of electron density $n(\mathbf{r})$ and potential $V(\mathbf{r})$.

2.1.9 Force evaluation

In DFT calculation, the force between ions is evaluated by using Hellman-Feynman theorem [44]. The calculated force is used for solving the Newton's equation of motion, molecular dynamics and geometry optimization. At a given pressure, we can find a set of atomic positions which gives the minimum energy by using geometry optimization. The step of solving an optimum point is controlled by the force tolerance. For stationary non-eigenfunction ψ (partial derivative is zero), the force on an interested ions at a position vector $\mathbf{R}_I$ can be calculated by

$$
\begin{aligned}
F_I &= -\frac{\partial E}{\partial R_I} = -\frac{\partial \langle \psi | H | \psi \rangle}{\partial R_I} \\
&= -\left\langle \psi \left| \frac{\partial H}{\partial R_I} \right| \psi \right\rangle - \left\langle \frac{\partial \psi}{\partial R_I} | H | \psi \right\rangle - \left\langle \psi | H | \frac{\partial \psi}{\partial R_I} \right\rangle \\
&= -\left\langle \psi \left| \frac{\partial H}{\partial R_I} \right| \psi \right\rangle - \varepsilon \frac{\partial \langle \psi | \psi \rangle}{\partial R_I} \\
&= -\left\langle \psi \left| \frac{\partial H}{\partial R_I} \right| \psi \right\rangle,
\end{aligned}
\tag{2.52}
$$

where E is the total energy calculated from the expectation value of Kohn-Sham Hamiltonian with Kohn-Sham orbitals. For algorithm of geometry optimization, the ions are firstly moved into new positions, and the electronic configuration is optimized. Next, the total energy is compared with previous configurations, and checked if forces lie within the tolerance limits. If the structure is not optimized, the procedure returns to the first step to generate a new set of ionic positions. Finally, the process is ended by checking if the total energy fall within the tolerance limits.

2.1.10 Absorption coefficient

In Cambridge Serial Total Energy Package (CASTEP), we can calculate the optical properties of solids that are due to electronic transitions. In general, the difference in the propagation of an electromagnetic wave through vacuum and some material can be described by a complex refractive index, N, which can be expressed in

terms of real part (n) and imaginary part (k) in the form $N = n + ik$. The absorption coefficient (η) is related to the imaginary part of refractive index k in form

$$\eta = \frac{2k\omega}{c} = \frac{4\pi k}{\lambda}. \tag{2.53}$$

Where λ is the wavelength in nm, which can be multiply by 10^7 to get the absorption coefficient in the units of cm^{-1}. The absorption coefficient depends on wavelength of photon, which has the energy above the band gap level. The probability of absorbing a photon depends on an electron transition from valence band to the conduction band. The inverse of the absorption coefficient is the absorption depth, which is the distance of penetration from the surface of material. For visible light region, the blue light (λ = 400nm) has a highest absorption, and it is absorbed in a short distance, while the red light (λ = 700nm) has a longest distance and low absorption.

For performing calculations of optical properties, it is common to evaluate the complex dielectric constant and then express other properties in terms of this. The complex dielectric constant, $\varepsilon(\omega) = \varepsilon_1 + i\varepsilon_2 = N^2$, where ω, ε_1 and ε_2 are the frequency of an incident wave, real and imaginary parts of the dielectric constant. In CASTEP, the imaginary part ε_2 of the complex dielectric constant can be calculated from

$$\varepsilon_2(\omega) = \frac{2e^2\pi}{\Omega\varepsilon_0} \sum_{\mathbf{k},v,c} \left| \left\langle \psi_{\mathbf{k}}^c \left| \mathbf{r} \right| \psi_{\mathbf{k}}^v \right\rangle \right|^2 \delta(E_{\mathbf{k}}^c - E_{\mathbf{k}}^v - E). \tag{2.54}$$

The ε_2 defined the transitions of electronic states with wave vector ($\mathbf{k}$) from valence state ($\psi_{\mathbf{k}}^v$) to conduction state ($\psi_{\mathbf{k}}^c$). The ε_1 can be obtained by the transformation of ε_2, which is called "*Kramers-Kronig transformation*" [45]. For solving the matrix elements, the position operator ($\mathbf{r}$) can be written in the momentum operator ($\mathbf{P}$) and their potentials. Moreover, the reflection coefficient and optical conductivity can be obtained from the complex dielectric constant.

2.2 Equation of States

From the solution of Kohn-Sham equations, we obtain a set of the total energy value (E) at an interested volume (V). It is well known that the total energy depends on the function of volume. We can find the equation of state (EOS) of a system from fitting the E-V curve. The most suitable model in solids is Birch–Murnaghan equation of state [46, 47]. In 1947, Murnaghan derived the Murnaghan equation of state from the relations in thermodynamics. Murnaghan assumed that the partial derivative of bulk modulus (B') is to be a constant and unchanged under high pressure as $B' = B_0'$. Therefore, the bulk modulus (B) can be written as $B = B_0 + B_0'P$, where B_0 and B_0', bulk modulus and their partial derivative at 0 GPa. The Murnaghan's EOS is obtained as

$$E(V) = E_0 + \frac{B_0 V}{B_0'}\left[\frac{(V_0/V)}{B_0' - 1} + 1\right] - \frac{B_0 V_0}{B_0' - 1}, \tag{2.55}$$

where E_0 and V_0 are the total energy and dependence volume at 0 GPa. The best fitting with E-V points by Eq. 2.55 was obtained from 4 suitable parameters. However, the usages of partials derivative in this equation is still incomplete. Later, Eq. 2.55 was developed by Birch and Murnaghan [47], published in 1947, in form

$$E(V) = E_0 + \frac{9B_0 V_0}{16}\left\{\left[\left(\frac{V_0}{V}\right)^{2/3} - 1\right]^3 B_0' + \left[\left(\frac{V_0}{V}\right)^{2/3} - 1\right]^2\left[6 - 4\left(\frac{V_0}{V}\right)^{2/3}\right]\right\} \tag{2.56}$$

and
$$P(V) = \frac{3B_0}{2}\left[\left(\frac{V_0}{V}\right)^{7/3} - \left(\frac{V_0}{V}\right)^{5/3}\right]\left\{1 + \frac{3}{4}(B_0' - 4)\left[\left(\frac{V_0}{V}\right)^{2/3} - 1\right]\right\}. \tag{2.57}$$

It is called "the third-order Birch–Murnaghan isothermal equation of state", derived in Ref [46] and [47]. Eq. 2.57 obtained from the first partial derivative of E with respect to V. For the isothermal solid-system, the third-order Birch–Murnaghan equation of state is suitable, but the percentage error between EOS and data points will be increased at very high pressure (more than 50 GPa). However, when studying up to extremely high pressure, the discrete pressure in all phase can be evaluated from the relation $P = -\Delta E/\Delta V$.

2.3 Determination of high pressure structures

The phase transitions of high pressure structures will be determined by using the 2nd laws of thermodynamics [48-49]. For a system in the isothermal surrounding, the entropy of universe (S_{univ}) is the combination of entropy of system (S_{sys}) and surrounding (S_{surr}). We have $\Delta S_{univ} = \Delta S_{sys} + \Delta S_{surr} \geq 0$. If Q is heat transferred from the surrounding (isothermal reservoir with temperature T) to the system, so the entropy change of the surrounding is $\Delta S_{surr} = -Q/T$. If the system is isobaric system, then $Q_P = \Delta H_{sys}$. It can be written as $\Delta S_{sys} + \left(-\Delta H_{sys}/T\right) \geq 0$ or

$$\Delta H_{sys} - T\Delta S_{sys} \equiv \Delta G_{sys} \leq 0. \tag{2.58}$$

In Eq. 2.58, it can be obtained by assuming that the temperature and pressure are constant. Therefore, Gibbs free energy $G_{sys} \equiv H_{sys} - TS_{sys}$ is defined for describing a system at both isothermal and isobaric. For chemical reaction, $\Delta G_{sys} < 0$ is favored reaction, while $\Delta G_{sys} = 0$ is equilibrium point of reaction. In DFT, we calculated at T=0 K; therefore, ΔG_{sys} will be reduced to the changing of enthalpy of system, ΔH_{sys}. The stable phase at a given pressure will be obtained from the minimum enthalpy structure [49, 50], shown in Figure 2.4. From E-V data points in each phase, it can be fitted by the 3rd order Birch–Murnaghan isothermal equation of state, shown as Figure 2.4 (a). We have the enthalpy in each phase, which are $H_1 = E_1 + P_1V_1$ and $H_2 = E_2 + P_2V_2$. E_1, E_2, V_1 and V_2 refer to internal energy and their volume of phase 1 and 2 at the point $H_1 = H_2$. At the transition pressure, we have the conditions $H_1 = H_2$ and $P_1 = P_2$, the transition pressure could be estimated from

$$P = -\frac{E_2 - E_1}{V_2 - V_1}. \tag{2.59}$$

Moreover, the transition pressure can be evaluated from the cross lines between H-P curves, shown in Figure 2.4 (b). The main problem for fitting EOS is the percentage error of P value. In this work, we have tested and found that the error for P (0-50 GPa) fitting by using the 3rd order Birch–Murnaghan equation of state is about 1 GPa

when compare with calculated from the nearly discrete points by using the relationship $P = -\Delta E / \Delta V$. At the phase transition, we can calculate the volume reduction between two phases. The types of phase transition can also be classified from this volume reduction plot. The first order phase transition can be suggested by its first energy derivatives shown discontinuous nature; while, the second order phase transition can be suggested by its continuous first energy derivatives but the second derivatives are discontinuous. In solids, the order of phase transition explained the mechanism of phase transition. The first order phase transition is explicitly reconstruction of the new structure, while the second order is the distortion between two closely related phases. We can also discuss the order of phase transition from *P-V* curve. The percentage of volume reduction defines the order of phase transition, shown in Figure 2.5.

(a)   (b)
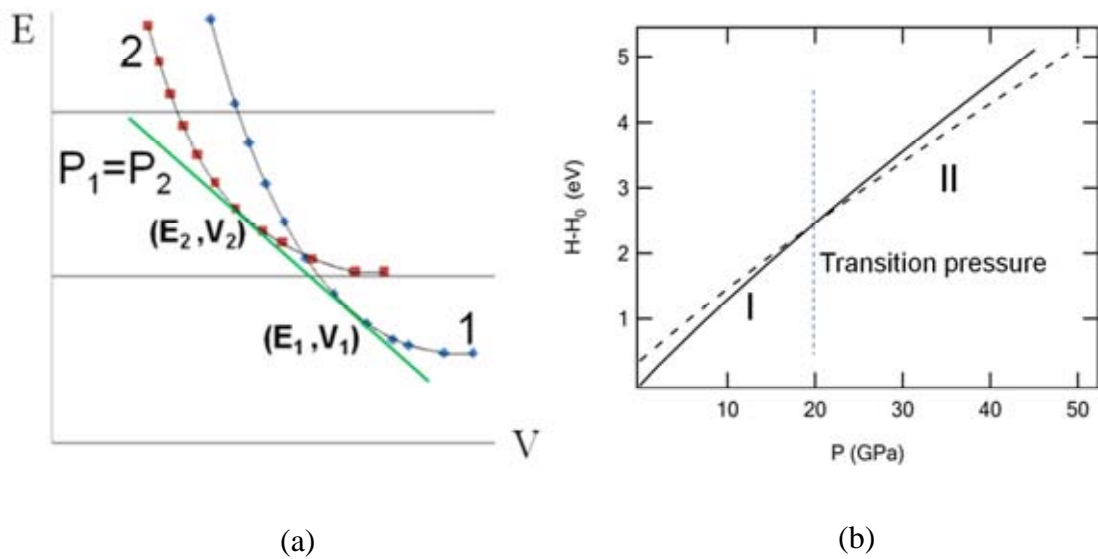
Figure 2.4: (a) The transition pressure from the example E-V curves fitting by EOS, while the *E-V* points are the solutions from KS equation. (b) The example of transition pressure at 20 GPa from the 1st (dash line) and 2nd (solid line) stable phases under high pressure.
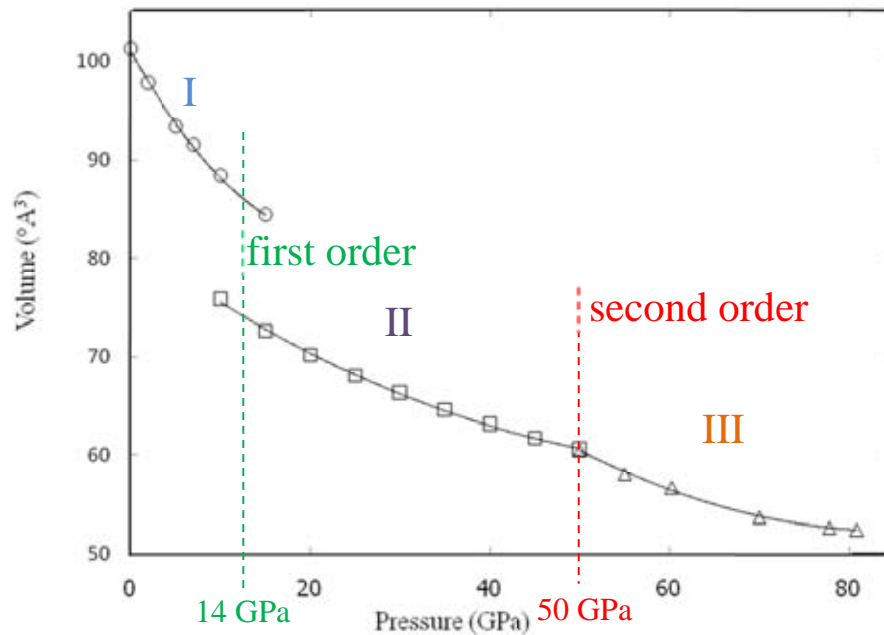
Figure 2.5: The example of *V-P* diagram shows the first order phase transition (I-II) 14 GPa and the second order phase transition (II -III) at 50 GPa.

2.4 Path of transformation

The phase transition can be determined by E-V or H-P curves. However, the mechanism during phase transition cannot be obtained from this. In the present work, we analyzed the path of transformation between cubic and orthorhombic phases. It is well known that *Cmcm* orthorhombic phase is the distorted structure of $Fm\overline{3}m$ cubic phase. At an interesting transition pressure, we have the initial and final structures, shown in Figure 2.6. We can approximate path of transformation by calculating energy at near the equilibrium point of two phases, shown in Figure 2.7, which are the potential wells. We can find the enthalpy (*H=E+PV*) from Y=0 to Y=0.2. Finally, we obtain the path of transformation and the barrier of transformation will be shown in chapter III.
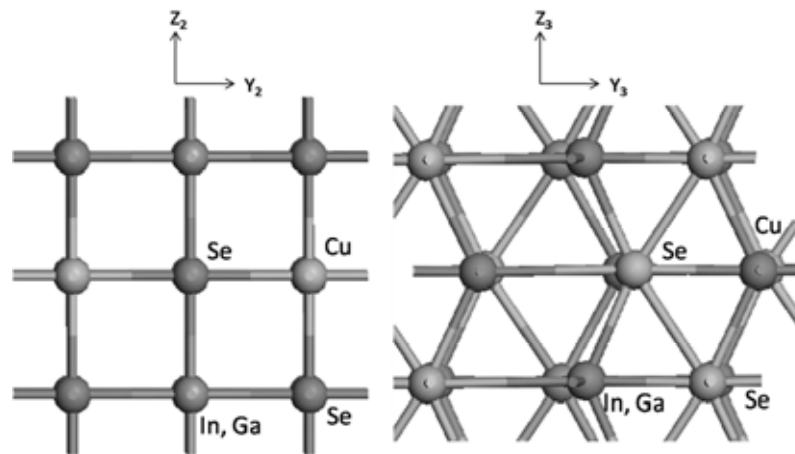
Figure 2.6: The distortion of *Cmcm* (right) from $Fm\overline{3}m$ (left) in Y axis.
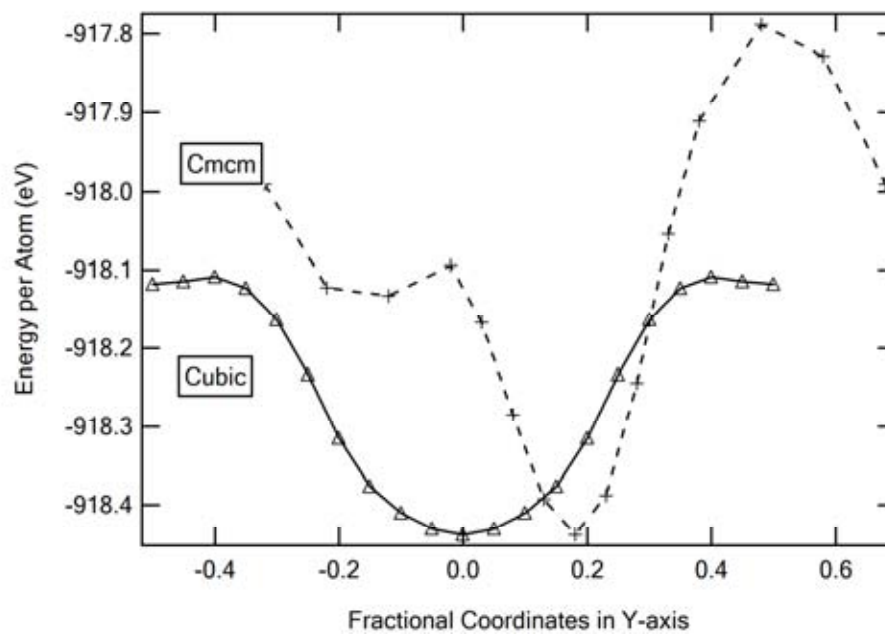
Figure 2.7: The potential (of cubic and *Cmcm* phases) from the equilibrium point.

In summary, we started from the origin of basic laws in physics or *ab initio*, and solving the Kohn-Sham solution to get the ground state properties at a given set of physical conditions. The EOS of a system can be obtained from the third-order Birch–Murnaghan equation of state. Finally, the stability of the proposed structure, phase transitions and their properties will be determined and evaluated under the laws of thermodynamics in the next part.

CHAPTER III

High Pressure Phases and Electronic Properties

DFT has been proved to be the most powerful tool for prediction physical properties in solids system as well as stability determination of high pressure phases [8]. In this work, the calculation has been focused on the semiconductor system under high pressure without the thermal effect (0 K). The results on *ab initio* calculation of high pressure phases as well as electronic properties of $CuInSe_2$ were presented in this chapter. The first phase transition of $CuGaSe_2$ was studied also. The main aim of the present research is to use *ab initio* method to study the structural phase transition of CIS, CGS and CIGS under high pressure. We reported the transition pressure and volume reduction, compared with experimental reports. We also gave description on the bonding under pressure. The band gap was estimated and the trend can be compared with existing experimental and other theoretical data. Furthermore, we proposed the path of transformation of CIS and CIGS from the $Fm\overline{3}m$ to $Cmcm$ structure. This allowed us to estimate the potential barrier between the two phases. This can provide a clue on the co-exist phases, reported by experiments [3].

3.1 Calculation details

In this work, the *ab initio* method was firstly calculated in CIS and CGS by using the self-consistent field (SCF) method as implemented in CASTEP code [51, 52]. From the SCF loops in Figure 2.1, all ground state properties are determined by solving Kohn-Sham equations from the DFT [52]. From the functional test, the results from widely used functionals, GGA and LDA, were compared. The results suggest that GGA is suitable for energy calculation and also any electronic properties for CIS, because the bulk modulus by using GGA gives a good agreement with the experimental report, shown in Table 3.1. The results of CGS are shown in Table 3.2 and 3.3 also. Therefore, the GGA-PBE functional [53, 54] was adopted for the exchange-correlation functional.

Table 3.1: The lattice parameters and bulk modulus of CIS by using GGA-PBE at 0 GPa, compared with those of experiments, LDA and FPLAPW theory.

Phase	a (Å)	c/a	B_0 (GPa)	Method
	5.7967	2.0071	54.45	GGA-PBE This work
	5.7783	2.0026		Expt. [3]
	5.733	1.988	53.22	FPLAPW-LDA [6]
$I\bar{4}2d$	5.782	2.009		Expt. [55]
			53.6	Expt. [56]
			70.92	LDA [57]

Table 3.2: Comparison of lattice parameters in chalcopyrite phase of CGS at 0 GPa with other works.

a (Å)	c (Å)	c/a	Method
5.618	11.196	1.993	GGA-PBE This work
5.542	10.840	1.957	LDA [6]
5.614	11.030	1.965	Expt. [58]
5.596	11.003	1.966	Expt. [59]

In most cases, the pseudopotential was used for assuming the potential of ionic cores, shown in Figure 3.1. For single point of total energy calculation and geometry optimization, the ultrasoft pseudopotential is a suitable potential because it requires the number of basis set or cutoff energy less than other methods such as norm conserving. The calculation results from ultrasoft pseudopotential were compared with other experimental report as well as another calculation technique, shown in Table 3.1, 3.2 and 3.3. GGA functional used pseudopotential model which saves computing time more than the full-potential linearized augmented-plane wave (FP-LAPW).
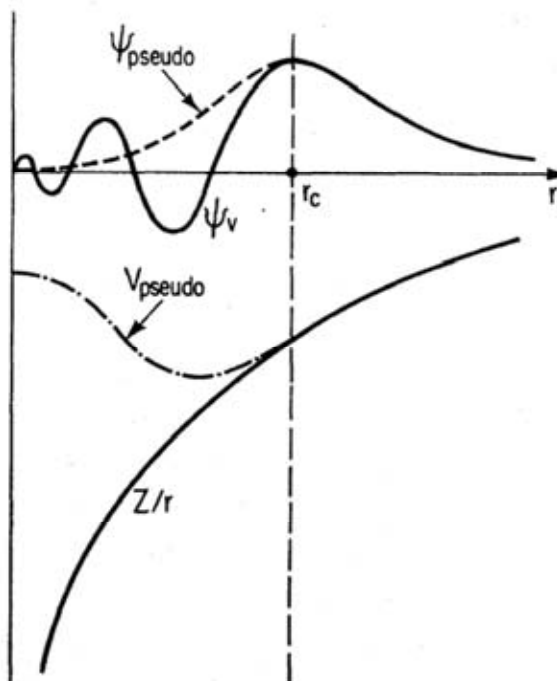
Figure 3.1: The scheme of all-electron (solid lines) and pseudoelectron (dashed lines) potentials and their corresponding wave functions. The radius r_c is the match of values [42].

Table 3.3: Comparison of CGS bulk modulus at ambient pressure (B_0) with other previous studies.

Compound	Method	B_0 (GPa)	Ref.
CGS	GGA PBE	66.23	This work
	LDA	57.84	[6]
	Theory	69.31	[60]
	Experiment	71.0	[56]
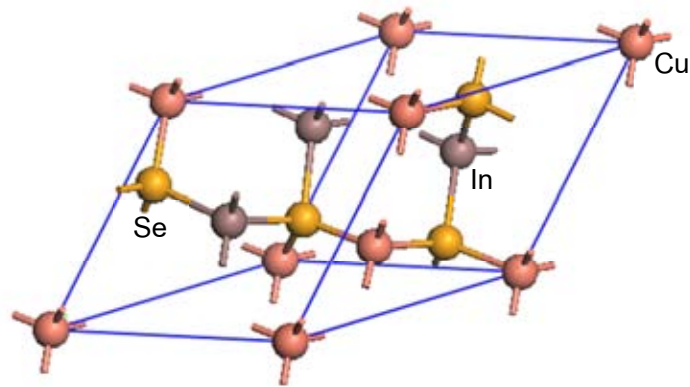
Figure 3.2: The examples of the primitive cell of CIS-$I\bar{4}2d$ at 0 GPa for total energy calculation.

The high pressure phases of CIS were taken from experiment [2, 3], which are the $I\bar{4}2d$, $Fm\bar{3}m$, and *Cmcm* structures. First of all, the primitive cell of $I\bar{4}2d$ at 0 GPa, shown in Figure 3.2, was observed the optimum parameters. The calculation parameters were optimized by convergent tests, and they are as follows; the cutoff energy was set to 500 eV for the total energy calculations, which the CIS energy difference between 500 eV and 700 eV is 3.25 meV/atom, shown in Figure 3.3 (a), comparison as $5\times5\times6$ k-point. The electron energy tolerance per atom was 0.01 meV. Monkhorst-Pack grid size for the SCF calculation was set to $5\times5\times6$ k-points (Figure 3.3 (b)) for $I\bar{4}2d$, and $5\times5\times5$ for $Fm\bar{3}m$ and *Cmcm* phases, which the total energy tolerance was controlled as less than 5 meV/atom. The total energy (E) is calculated as a function of their volume (V). The E-V data points were fitted to the 3rd order Birch-Murnaghan equation of state (EOS) [46, 47]. The stability of the high pressure phases was determined from the lowest enthalpy, $H = E + PV$. We calculated the CIS energy gap and the electronic band structure at each pressure by using sX-LDA with $3\times3\times4$ k-points, cutoff energy of 800 eV. In CASTEP code, the sX-LDA calculation supports only the norm-conserving pseudopotential. We also used a higher cutoff energy at 880 eV, and it gave a slightly different total energy within the range of 5 meV/atom.

(a)

(b)
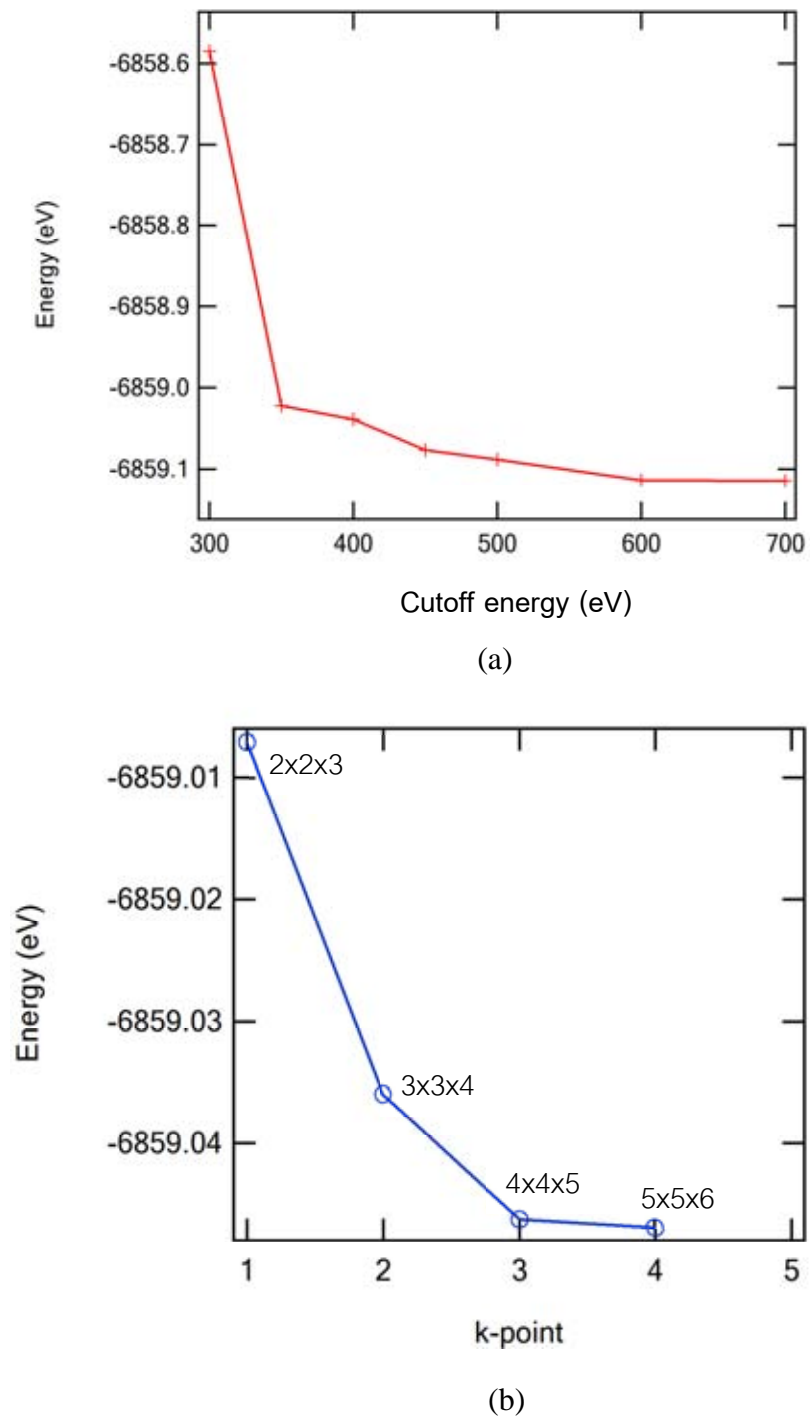
Figure 3.3: (a) The cutoff energy of CIS-$I\bar{4}2d$ at 0 GPa being tested up to 700 eV, and (b) The examples of k-point sampling in CIS-$I\bar{4}2d$ being tested at $2\times2\times3$, $3\times3\times4$, $4\times4\times5$, $5\times5\times6$ respectively.

3.2 High pressure phases results

In order to verify our calculation, we calculated the $I\bar{4}2d$ structure in CIS and CGS at 0 GPa and compared with the existing theoretical and experimental data, as shown in Table 3.1 and 3.2. E-V data points of the different phases in CIS and CGS were calculated and fitted to the EOS, as shown in Figure 3.4 and 3.5. The E-V curves showed that the $I\bar{4}2d$ phase has lowest energy at equilibrium volume. The lowest energy has shifted to the $Fm\bar{3}m$ as volume decreased. For CIS, it was studied up to 80 GPa and found the $Cmcm$ structures, while CGS was studied only the first transition ($I\bar{4}2d \rightarrow Fm\bar{3}m$). All stable phases were observed by using the enthalpy (H) as a function of pressure (P). The Figure 3.5(b) is the enthalpy difference, using the CIS-$I\bar{4}2d$ enthalpy as a reference. The H-P curve clearly showed that CIS with the $I\bar{4}2d$ structure transforms into the $Fm\bar{3}m$ structure at 12 GPa, and then to the $Cmcm$ structure at 42 GPa. In addition, we plotted the volume-pressure relation, as shown in Figure 3.4(b) (CGS) and 3.6 (CIS). These relations provided the information on the volume reduction at each phase transitions. We found that the CIS volume reduction at the $I\bar{4}2d$ to $Fm\bar{3}m$ transition is 13.9%, and at the $Fm\bar{3}m$ to $Cmcm$ transition is 1.9%, compared with 11% and 1% respectively from the experiments [2, 3]. From the order of stable phases and the trend of volume reductions, it is readily seen that the calculation gave good description to the experiment [3].

For CGS calculations, after it was optimized at 0 GPa, atomic coordinates of Cu, Ga and Se are (0, 0, 0), (0, 0, 0.5) and (0.244, 0.25, 0.125) respectively. The average minimum energy per atom (E_0) is -980.469 eV at the volume of 22.005 $\mathring{A}^3$. The bulk modulus in chalcopyrite phase of CGS at minimum energy point or ambient pressure is 66.23 GPa which has been compare with previous studies in Table 3.2. From Table 3.2 and 3.3, one can conclude that DFT calculation is relatively reliable tool for ground state energy calculations. The enthalpy of $I\bar{4}2d$ and $Fm\bar{3}m$ structures is equal at 19.77 GPa, shown in Figure 3.4(a). At this point, the average volumes per atom of the two phases are 18.123 and 15.487 $\mathring{A}^3$ for tetragonal and cubic respectively. Therefore, the first phase transition can be predicted at this pressure which accompanies a volume reduction of 14.54 %, shown in Figure 3.4(b).

When compare with the experimental data using energy dispersive x-ray diffraction (EDX) of T. Tinoco *et al*. [60], they have reported the transition pressure at 13 GPa and volume difference is 13 %.

The transition pressures and the volume reductions of CIS and CGS were summarized and compared with existing data from the experiment [3] and [60] in Table 3.4. Moreover, the transition pressure of CIGS was also compared. The details of CIGS structural phase transition and effect of Na on the phase transitions in CIGS will be fully explained in chapter 4. The predicted transition pressure obtained from this calculation appears to be higher than the experimental results (see in Table 3.4). This can be explained by the effect of our simulation setup. In order to simulate the homogenous distribution of Cu and In in space groups $Fm\bar{3}m$ and *Cmcm*, the symmetry imposed by atoms at the occupancy site can vividly higher than the real crystal. This would affect the total energy in both structure and hence transition pressure. In the real crystal, the distribution of both Cu and In site should have less symmetry. Therefore, the total energy at each volume points should be less than those approximated in the calculation and the predicted transition pressure should also be lower. In addition, the small discrepancy was occurred due to the fact that our DFT phase transition was calculated at low temperature which still neglects thermal effect.
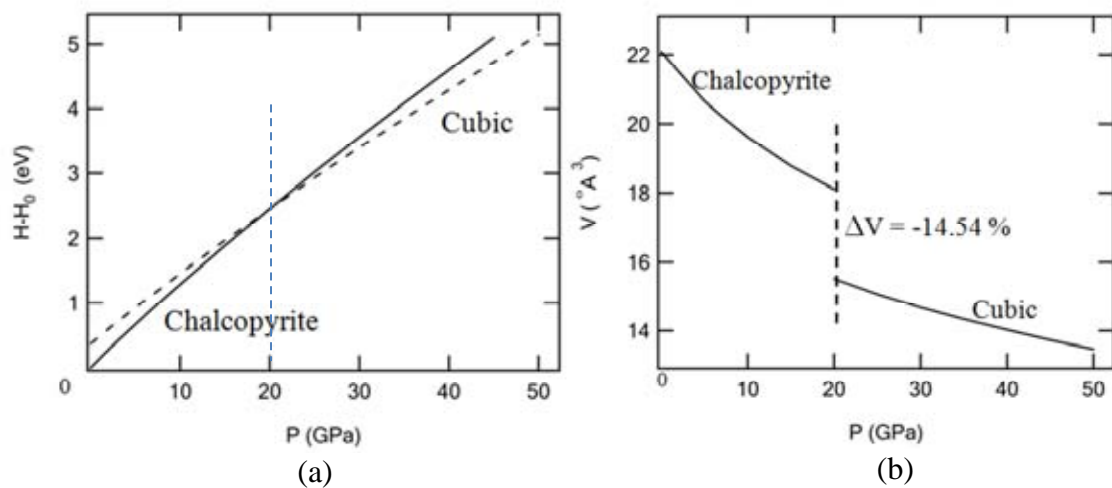
Figure 3.4: (a) The relation between H – H_0, the difference enthalpy of high pressure and chalcopyrite phase of CGS at 0 GPa, with pressure (P) 0 – 50 GPa. (b) P-V diagram of CGS bet ween chalcopyrite and NaCl-like cubic phases which reduced volume is 14.54 %.
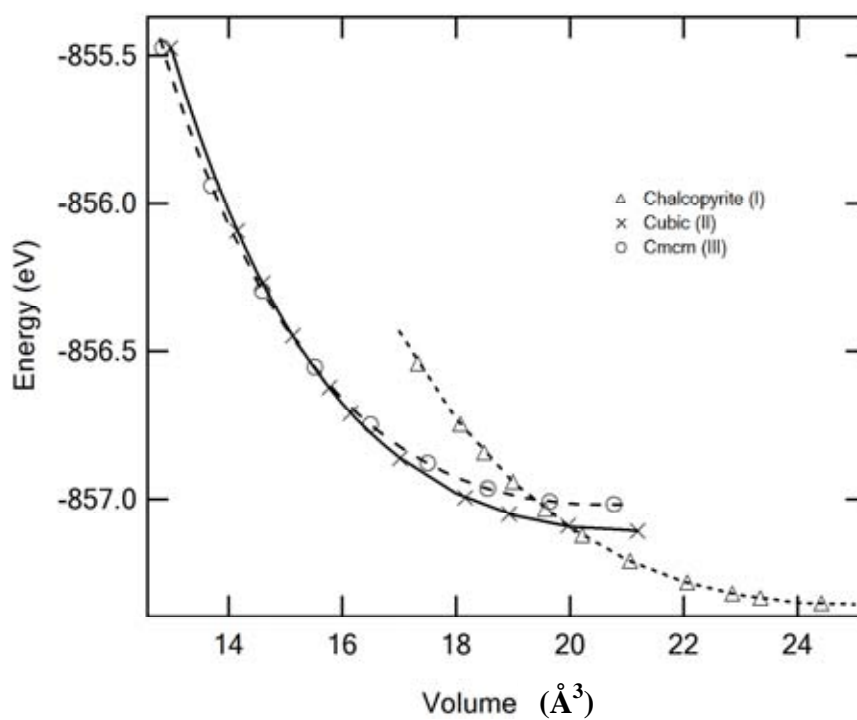
(a)
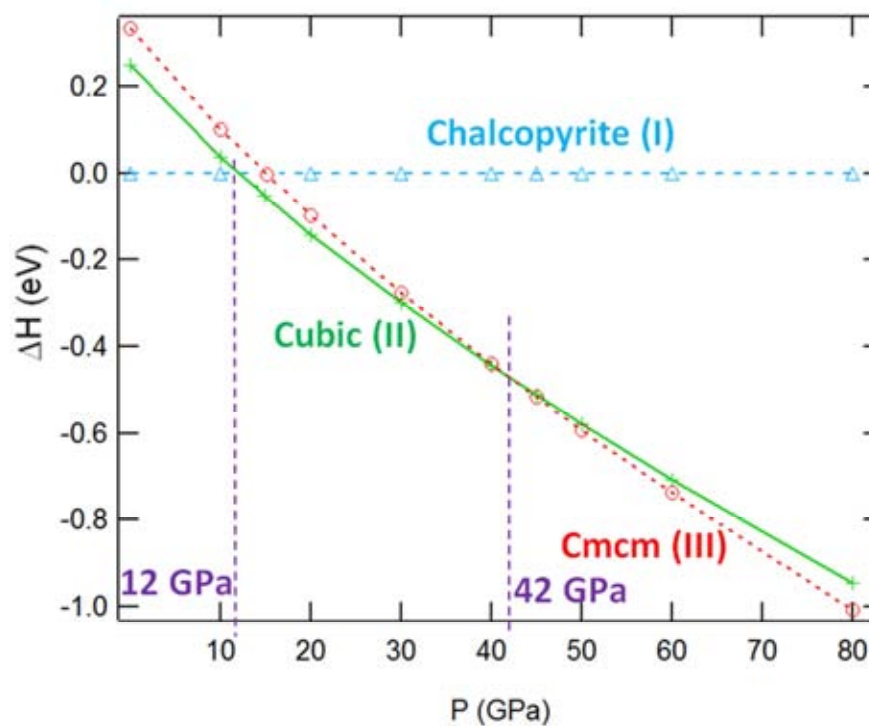
(b)

Figure 3.5: (a) E-V data points of the three phases and their fitted EOS. (b) The markers are the enthalpy difference as a function of pressure, while the beelines link between two markers. The enthalpy of chalcopyrite phase was used as a reference.
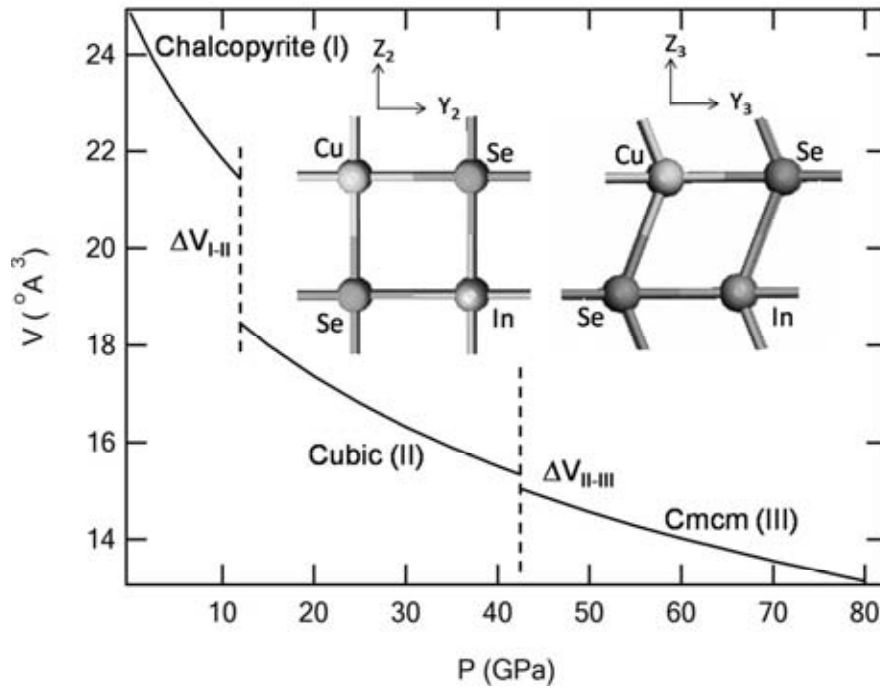
Figure 3.6: The equations of states (V-P relation) of the three phases of CIS between 0–80 GPa. This V-P curve allowed us to find the volume reduction at each phase transitions. The inset showed the atomic movements as CIS transforms from the $Fm\bar{3}m$ to $Cmcm$ structure.

Table 3.4: Summary of the transition pressure and the volume reduction of CIS, CGS and CIGS at each phase transitions, compared with the CIS and CGS experimental data in parentheses from Bovornratanaraks *et al*. [3] and Tinoco *et al*. [60] respectively.

Material	Transition Pressure (GPa)	$-\Delta V$ (%)	Phase Transition
CIS	12 (7)	13.9 (11)	$I\bar{4}2d$ to $Fm\bar{3}m$
	42 (39)	1.9 (1)	$Fm\bar{3}m$ to $Cmcm$
CGS	20 (13)	14.5 (13)	$I\bar{4}2d$ to $Fm\bar{3}m$
CIGS	13	14.2	$I\bar{4}2d$ to $Fm\bar{3}m$
	24	2.2	$Fm\bar{3}m$ to $Cmcm$

3.3 Path of transformation in CIS and CIGS

From the CIS structures calculation, we obtained also the optimized atomic positions of each phases. The $Fm\overline{3}m$ and *Cmcm* atomic positions of CIS in the YZ plane were shown in the inset of Figure 3.6. The atomic visualization in the inset allowed us to construct the path of transformation from the $Fm\overline{3}m$ to *Cmcm* structure. First, the Cu-Se layers in XY plane moves relatively parallel to the In-Se layers. The magnitude of the relative atomic movement is 20% in the Y axis. Second, the phase transition also involves some small strain because the shape of the unit cell changes and volume reduces during the phase transition. By taking all these changes into the account, we calculated the enthalpy along the path by starting at the perfect $Fm\overline{3}m$ phase and moving the Cu-Se layer along the Y axis at each step by 0.05 in the reduced cell units. During the movement of Cu-Se layer in Y axis, the pressure on a system is still unchanged in all steps. After a few movement steps, the phase transition is completed and the *Cmcm* structure was obtained. The result of the enthalpy along the transformation path was shown in Figure 3.7. Hence, our simulated path of transformation has provided the upper bound to the barrier between the two phases. It is an upper bound because the exact path of transformation will always have lowest enthalpy.
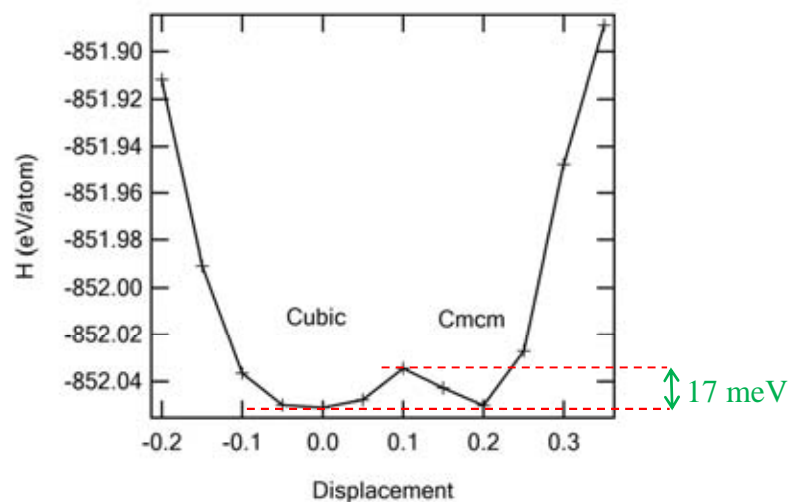
Figure 3.7: The enthalpy along the path of transformation. It showed the two distinguish energy wells of the NaCl-like cubic and the *Cmcm* phases, and also the barrier of 17 meV, equivalent to 198 K.

From Figure 3.7, we found that the barrier height is 17 meV per atom or equivalent to the thermal energy at 198 K. This finding can be used to explain the co-existence of the $Fm\bar{3}m$ and *Cmcm* phases. In fact, this co-existence was reported in the x-ray diffraction experiment [3] that the *Cmcm* structure firstly appeared at 33.9 GPa in the $Fm\bar{3}m$ phase, then they co-existed in the pressure range of 33.9-43.9 GPa. The complete phase transition to the *Cmcm* structure occurred at 43.9 GPa onward.
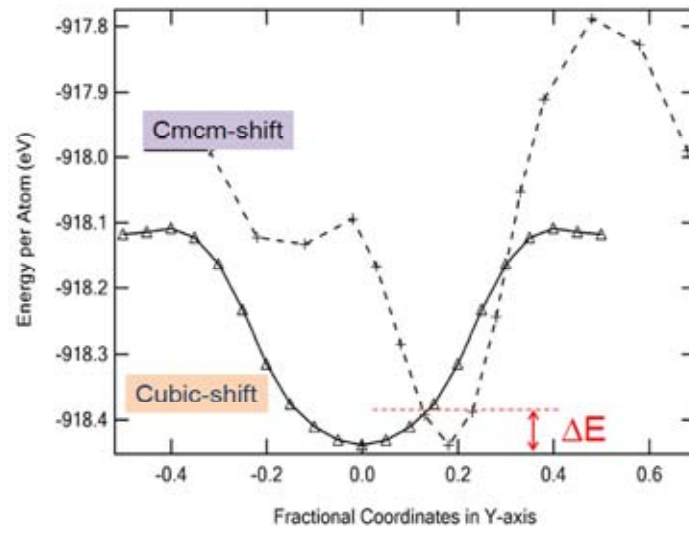
Figure 3.8: The potential wells of cubic ($Fm\bar{3}m$) and orthorhombic (*Cmcm*) phases at nearly transition pressure between two phases.
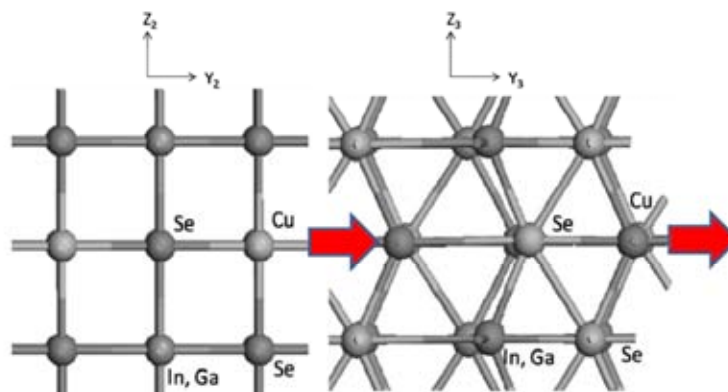
Figure 3.9: The path of distortion and the atomic positions of $Fm\bar{3}m$ and *Cmcm*.

For mechanism of distortion in CIGS, The shape of CIGS potential of $Fm\bar{3}m$ and *Cmcm* were tested, shown in Figure 3.8. The x-y plane was displaced from the equilibrium position. The $Fm\bar{3}m$ phase shows symmetric potential, while the *Cmcm* phase gives a non-symmetric potential. The left handed side of *Cmcm* potential is

lower than the right handed side. This result supports the transformation path in Figure 3.8. The cross lines between two potential from different structure shows the maximum barrier of their phase transition. Nevertheless, this value still neglects the effect of volume reduction. From Figure 3.9, we can estimate the transformation path from $Fm\bar{3}m$ to $Cmcm$ structure. We found that the Cu-Se plane (xy plane in Figure 3.9) of the $Fm\bar{3}m$ structure was displaced along the y-axis, parallel to the (In,Ga)-Se plane, which this gives cubic-orthorhombic distortion. The relative plane movement is about 18%. We also took the volume reduction and unit cell distortion into the account. We calculated the enthalpy along the estimated path at 25 GPa, close to the $Fm\bar{3}m$ to $Cmcm$ phase transitions. From the enthalpy curve, we found that there were two energy wells with one barrier, as shown in Figure 3.10. The wells located the local stability of the $Fm\bar{3}m$ and $Cmcm$ structures accordingly. The barrier which separates the two well has the magnitude of 0.020 eV/atom, which is equivalent to thermal energy at 248 K. In addition, we found that 0.1%, 1.0% and 6.25% Na have a little effect on the shape and magnitude of the barrier.
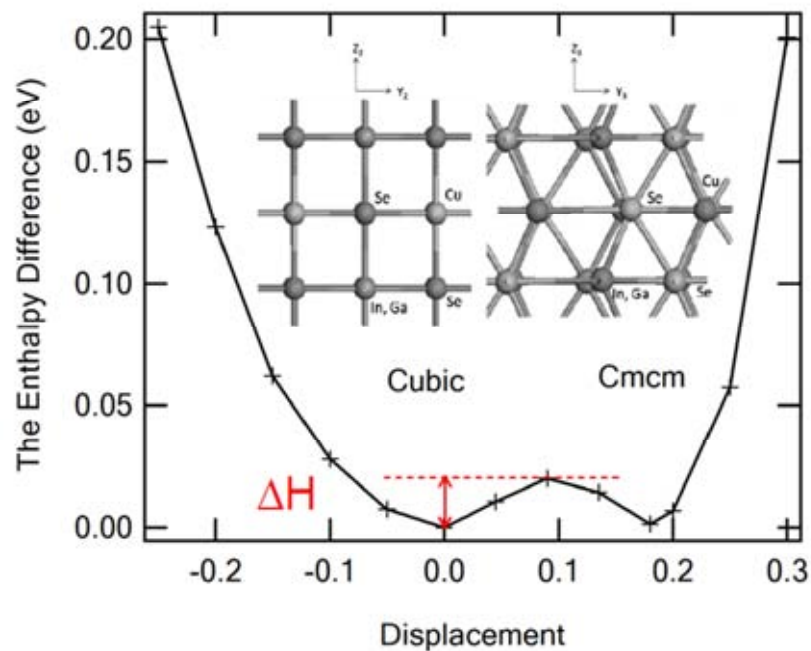
Figure 3.10: The enthalpy along the estimated transformation path from $Fm\bar{3}m$ to $Cmcm$ structure of pure CIGS at 25 GPa. The Cu-Se (xy) plane was translated along the y-axis relatively to the (In,Ga)-Se plane by 18%.

Table 3.5: The CIS band gap from sX-LDA and the trend of gap under pressure, compared with FPLAPW [6], LDA [61], sX-LDA [7] and experimental results [4, 5].

Structures	Band Gap (eV)	$\Delta E_g/\Delta P$ (meV/GPa)	Method
	0.680	39.6	sX-LDA[a]
	0.913 (5 GPa)	39.6	sX-LDA[a]
	1.076 (10 GPa)	39.6	sX-LDA[a]
$I\bar{4}2d$	0.98	30	Expt.[b]
(0 GPa)	1.04	29	Expt.[c]
	0.26	-	FPLAPW-LDA[d]
	0.96	-	sX-LDA[e]
	0.12	31	LDA[f]
$Fm\bar{3}m$ (15 GPa)	Vanish	-	sX-LDA[a]
$Cmcm$ (50 GPa)	Vanish	-	sX-LDA[a]

[a]This work.

[b]Reference 4.

[c]Reference 5.

[d]Reference 6.

[e]Reference 7.

[f]Reference 61.

3.4 Band structure of CuInSe$_2$

Next, we calculated the band gap of the three phases. It is widely known that the local scheme of DFT gives good description on the ground state of the system only. However, the energy gap calculation involves the excitation states and the local exchange-correlation functional can be inaccurate. It is also well known that the typical GGA band gap is inaccurate, shown in Figure 3.11. Thus, we resorted to sX-LDA functional. It uses non-local screened exchange scheme combining with LDA correlation functional, and should provide a better energy functional than the pure local scheme of the LDA or GGA [7]. Indeed, our gap values were in fair agreement

with experimental data and other theoretical studies. We found that the sX-LDA band gap at 0 GPa is 0.680 eV in the chalcopyrite ($I\bar{4}2d$) phase, and the band gap increases as pressure increases. The band gap is improved by sX-LDA; however, it is still underestimated from experiment value due to excluding another effect of excited state. The increase rate of the band gap is 39.6 meV/GPa, compared with 30 meV/GPa from optical absorption experiment [4-5, 61]. In the $Fm\bar{3}m$ and *Cmcm* phases, the band gap vanishes because of the overlap between the valence band maximum (VBM) and the conduction band minimum (CBM), shown in Figure 3.12(b). The electronic density of states (EDOS) also suggests the transition from semiconductor to metallic. Typical band structures of the $I\bar{4}2d$ and $Fm\bar{3}m$ structures were shown in Figure 3.12(a) and (b). The results of the sX-LDA gap values were summarized in Table 3.5. The error in the DFT band gap value is seen that it is systematic error. Zhang *et al* [61] showed that the band gap of CIS at 0 GPa is 0.17 eV from LDA but it can be corrected by a adding constant shift of 1.04 eV from experiments. Similarly, Vidal *et al.* [8] also showed that CIS the DFT gap tendency closely resembles the more accurate GW gap tendency.
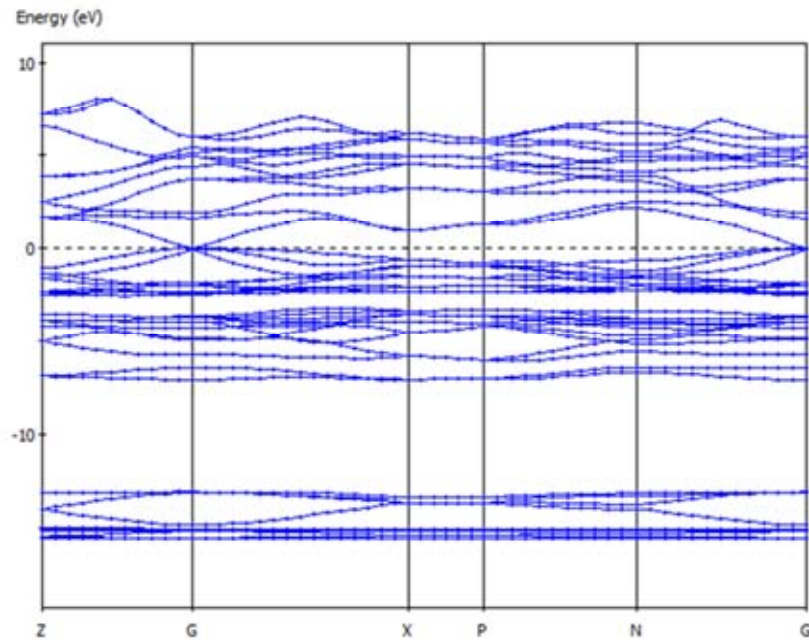
Figure 3.11: The CIS band structure at 0 GPa calculated from GGA-PBE.
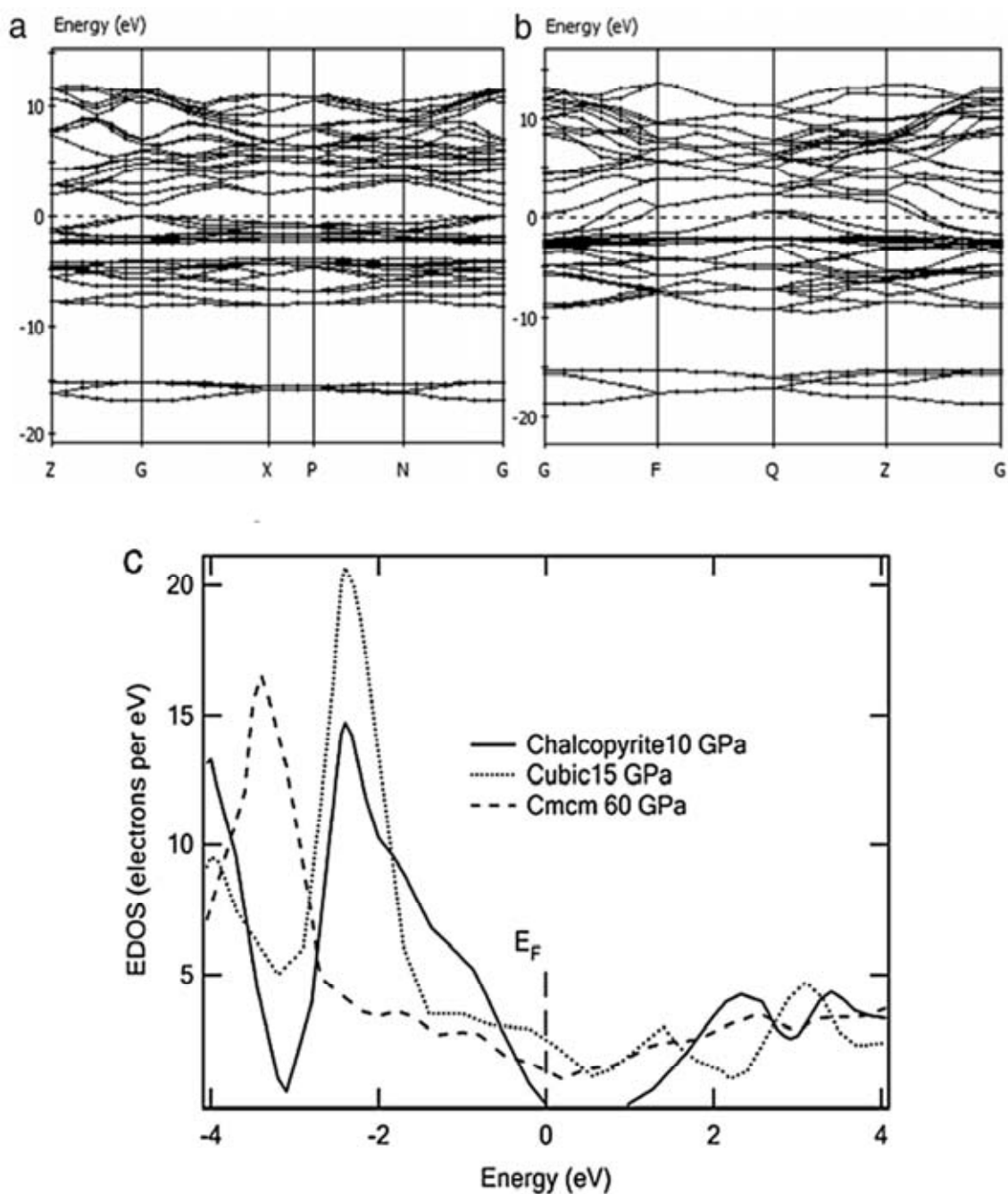
Figure 3.12: Comparison the energy bands of CIS from sX-LDA. (a) The energy band of the chalcopyrite phase at 5 GPa with the gap of 0.913 eV. (b) The energy band of the NaCl-like phase at 15 GPa. The VBM and CBM are overlapped. The Fermi level was set as references at 0 eV. (c) Comparisons the electronic density of states (EDOS) of high pressure phases.

(a)

(b)

(c)
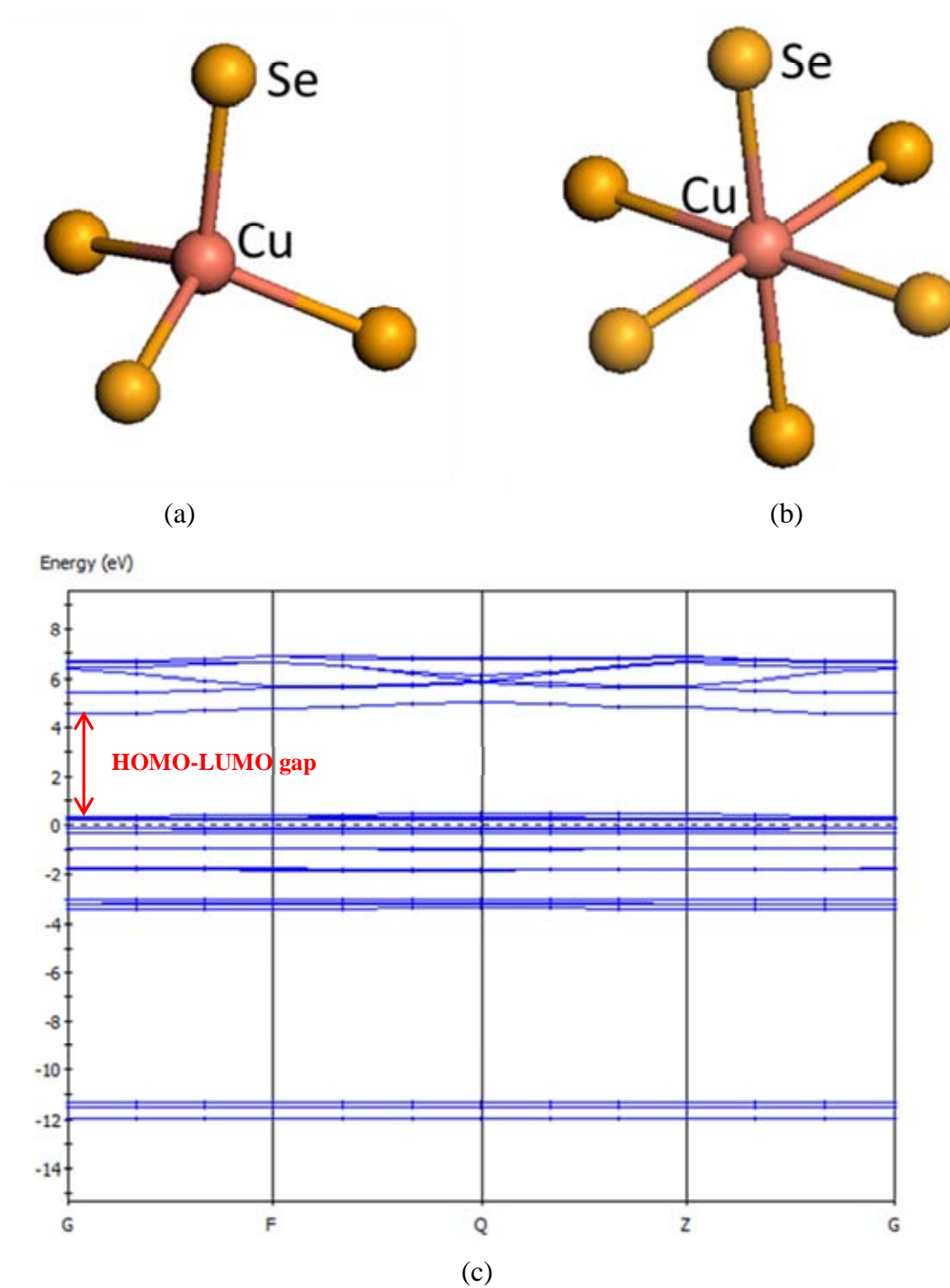
Figure 3.13: (a) and (b) show the isolate molecules $CuSe_4$ and $CuSe_6$ respectively. (c) the example of HOMO-LUMO gap of isolate molecule.
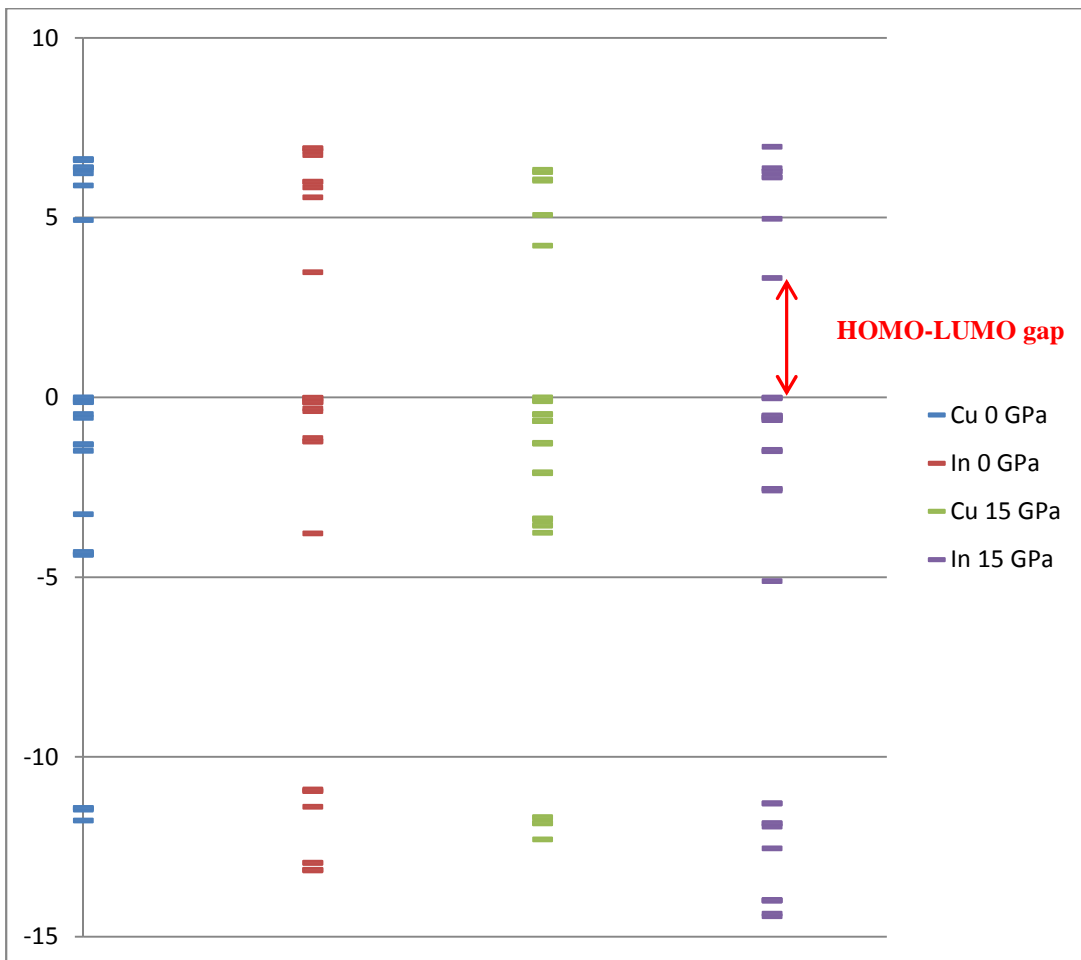
Figure 3.14: Comparisons The HOMO-LUMO gap of $CuSe_4$, $InSe_4$, $CuSe_6$ and $InSe_6$ in $I\bar{4}2d$ phase at 0 GPa and cubic phase at 15 GPa respectively.

Table 3.6: The bond length of the closest Cu-Se and In-Se pairs under high pressure.

	P (GPa)					
Bond length (Å)	$I\bar{4}2d$			$Fm\bar{3}m$		$Cmcm$
	0	5	10	15	40	60
Cu-Se	2.42	2.36	2.31	2.64	2.48	2.50
In-Se	2.65	2.59	2.55	2.64	2.47	2.45

Table 3.7: The population analysis (fractional number of electrons) of CIS in $I\bar{4}2d$ (0, 5 and 10 GPa), $Fm\bar{3}m$ (15 and 40 GPa) and $Cmcm$ (60 GPa).

P	Cu			In			Se	
(GPa)	s	p	d	s	p	d	s	p
0	0.68	0.80	9.8	1.30	1.37	9.99	1.56	4.47
5	0.68	0.84	9.8	1.26	1.41	9.99	1.54	4.47
10	0.68	0.87	9.79	1.24	1.45	9.99	1.51	4.48
15	0.72	0.74	9.75	1.34	1.36	9.99	1.6	4.44
40	0.73	0.78	9.75	1.29	1.42	9.98	1.58	4.44
60	0.79	0.88	9.78	1.26	1.58	9.97	1.54	4.34

In addition, we have investigated the bond length and its relation to the band gap. Maeda and Wada [7] explained that the valence band of CIS is dominated by Cu *3d* and Se *4p* whereas the conduction band is dominated by In *5s* and Se *4p*. They also showed that in an isolated $CuSe_4$ or $InSe_4$ molecule, the energy levels split due to covalent bonding, shown in Figure 3.13 and 3.14. The key feature is that the proximity of atoms in the molecule strengthens the bonding, and the energy levels split further apart. Then, they replaced the In atom by a Ga or Al atom and found that the III-VI bonds are shortened. These shortened bonds are accompanied by the widening band gap in the bulk I-III-VI compounds as expected. This situation is similar to CIS under high pressure where all the bonds are shortened, see Table 3.6, and the band gap is widened in the $I\bar{4}2d$ phase (0-12 GPa). Thus, this is just the effect of the stronger bonding under high pressure. However, at the $I\bar{4}2d$ to $Fm\bar{3}m$ phase transition, the Cu-Se and In-Se bonds suddenly become longer. This is surprising at first because we would expect a more packed structure under high pressure. By looking closely at the $I\bar{4}2d$ structure, we found that a Cu atom is coordinated by 4 Se atoms, similar to an In atom which is also coordinated by 4 Se

atoms. After the phase transition to the $Fm\bar{3}m$ structure, the Cu atom is coordinated by 6 Se atoms, so as the In atom. The volume of unit cell per formula unit of CIS is reduced by 14% from phase transition, but the bond lengths in the unit cell are increased due to the characteristic of space group. Thus, the total structure is still more packed under pressure, even though the bond lengths are longer. In order to understand the gap closure at the $I\bar{4}2d$ to $Fm\bar{3}m$ phase transition, we look at the isolated molecules of $CuSe_4$ and $InSe_4$ which constituent the $I\bar{4}2d$ structure and the isolated $CuSe_6$ and $InSe_6$ which constituent the $Fm\bar{3}m$ structure. The $CuSe_4$ and $InSe_4$ are a tetrahedral molecule, whereas the $CuSe_6$ and $InSe_6$ are an SF_6-type molecule, shown in Figure 3.13(a) and (b). The HOMO-LUMO gap (see in Figure 3.13(c) and 3.14) can be used to indicate the strength of bonding. From our DFT-GGA calculations, we found that at 0 GPa, the $CuSe_4$ and $InSe_4$ molecules have HOMO-LUMO gap of 4.94 eV and 3.49 eV respectively. At 15 GPa, the $CuSe_4$ and $InSe_4$ have HOMO-LUMO gap of 4.84 eV and 4.33 eV respectively, whereas the $CuSe_6$ and $InSe_6$ have HOMO-LUMO gap of 4.22 eV and 3.33 eV respectively. The significant changes can be noticed from the $InSe_x$ molecules. For the $InSe_4$, the HOMO-LUMO gap is widened under pressure. Nevertheless, at close to the phase transition, the HOMO-LUMO gap has changed from 4.33 eV in the $InSe_4$ to 3.33 eV in the $InSe_6$, shown in Figure 3.14. When these molecules form a bulk CIS, the solid band gap would be reduced accordingly. It is worth noting that the energy levels in the $CuSe_x$ molecules are less sensitive to the bond reduction. This is because the bonding in the I-VI is much weaker than in the III-VI. The population analysis of CIS in chalcopyrite was analyzed in Table 3.7. It shows that CIS has *s-p* hybridization.

3.5 Photoabsorption of CuInSe$_2$

From the Kohn-Sham orbitals and complete Hamiltonian, we can evaluate the real and imaginary parts of the dielectric constant (ε), shown in Figure 3.15(c). Most of important optical properties such as refractive index, reflectivity and photoabsorption can be obtained from the imaginary parts of the dielectric constant. The GGA-PBE optical band structure, shown in Figure 3.15(a), gives a higher band gap than the electronic band structure. This is because it has been calculated using random k-point, which not along the high symmetry of 1st BZ. The electronic band

structure is focused on valence band maximum (VCM) and conduction band minimum (VBM) at the gamma point and another symmetry point, while the optical band structure is focused on the average transition between valence band and conduction band. The optical band gap will be converged to the electronic band gap at very high k-point sampling. However, the higher band gap in the optical band structure is suitable for calculating the optical properties. But the accuracy of the optical properties outcome from optical band gap is still discussed. The optical band gap increased at the rate 24 meV/GPa in chalcopyrite phase.
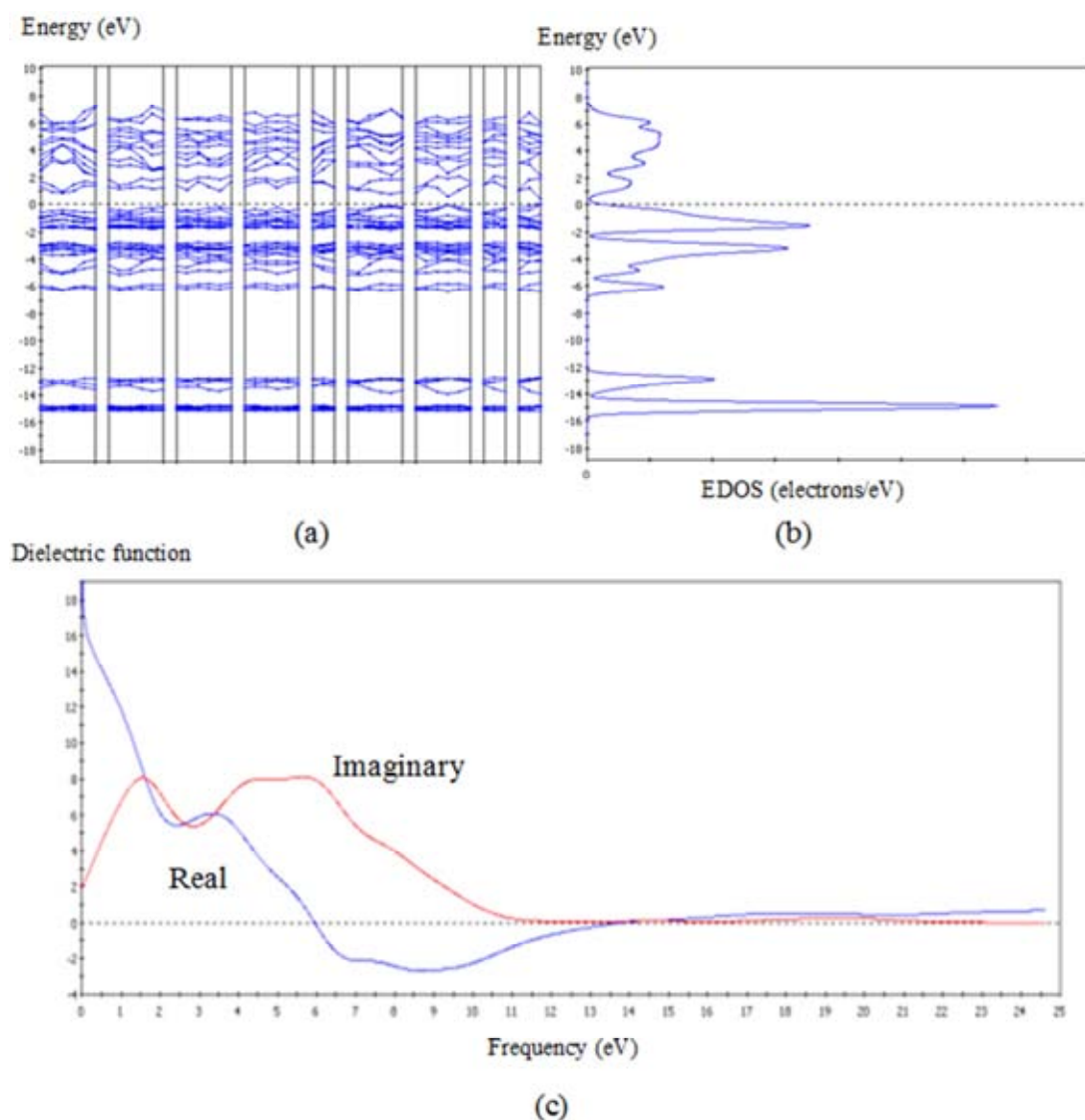
Figure 3.15: (a) The calculated GGA-PBE optical band gap of CIS at 0 GPa. (b) The electronic density of state obtains from the integral of band structure. (c) The calculated dielectric function in real part (blue) and imaginary part (red).

Table 3.8: The optical band gap and photoabsorption of CIS calculated from GGA-PBE at 0, 5 and 10 GPa.

Properties\Pressure	0 GPa	5 GPa	10 GPa
Optical band gap (eV)	0.380	0.503	0.612
The best absorp. (nm)	134	127	124
Absorp.at 400 nm (counts)	52000	54000	54000
Absorp.at 700 nm (counts)	37500	33000	28000
Max absorp. (eV)	22.5	23.0	23.5
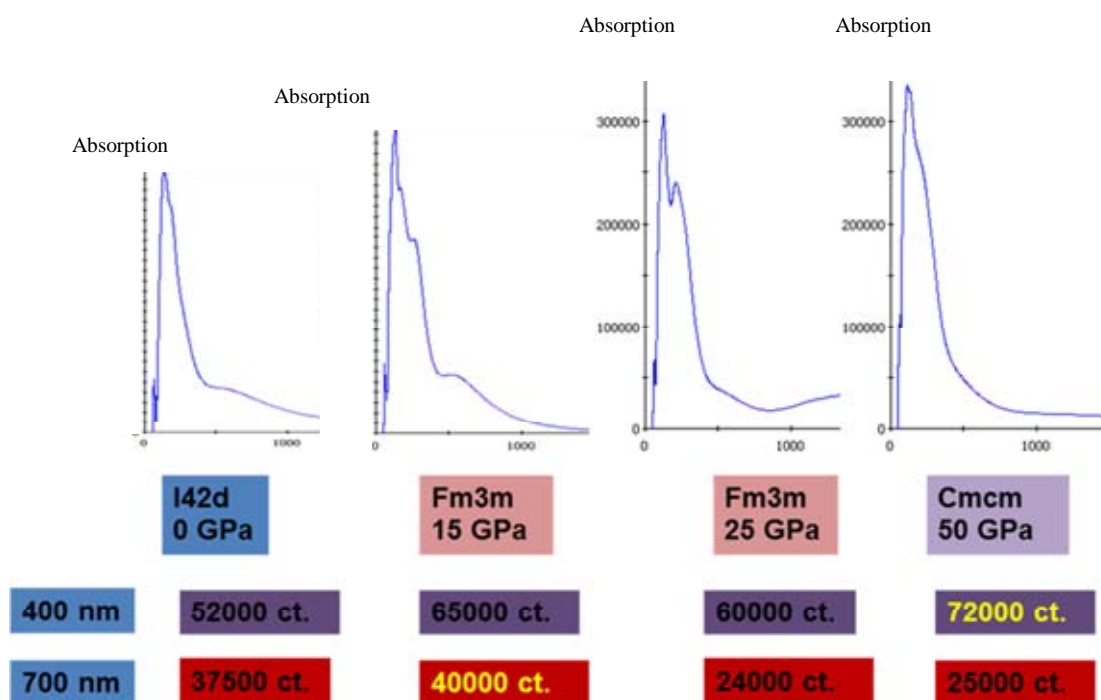
Figure 3.16: Comparisons photoabsorption of CIS in all phases calculated from GGA-PBE at 400 and 700 nm.

In this research, the best absorption of CIS at 0, 5 and 10 GPa are predicted 134, 127 and 124 nm respectively. The result is shown in Table 3.8. The incorrect band gap is a cause of underestimation in wavelength-absorption. The visible light absorptions at 400 and 700 nm has been calculated. In chalcopyrite phase, the CIS photoabsorption at 400 nm increased by 3.7% at 5 GPa. But it decreased by 12% with the pressure increasing. The photoabsorption has been studied up to 50 GPa in *Cmcm* phase and the results is shown in Figure 3.16. From this result, the trend of photo absorption cannot be predicted. However, the result indicates that the highest absorption occurred in high pressure non-semiconducting phase. Therefore, it cannot be applied for solar cell materials. From studying photoabsorption in CIS, it was found that the band gap obtained from GGA-PBE (or LDA) is found to be inaccurate and not suitable for explaining the true optical properties.

CHAPTER IV
Na Effects on CIGS High Pressure Phases

From previous chapter, the CIS ternary compound has been fully investigated for stability of the proposed structure under high pressure as well as their phase transition and electronic. In this chapter, the investigation has been extended to quaternary compound, and the doped semiconductor. This simulation can be performed by incorporation of the impurity atoms. The study will be focused on the most widely used impurity-atom for the photovoltaic materials which is $CuIn_{0.5}Ga_{0.5}Se_2$ or CIGS. The achievement of higher efficiencies can be obtained by adding a small amount of Na into CIGS. This was supported by several previous experimental reports [9-19]. In simulation works, the incorporation of Na into CIS was first analyzed by Wei *et al.* [18] and Li *et al.* [19]. Li *et al.* applied a supercell method and replaced a Na atom on one of the Cu sites (Na_{Cu}). They observed that at the concentration of 6.25% Na atom, Na_{Cu} increases the CIS band gap by 0.114 eV at ambient pressure. Another effect is to increase the density of states near valence band maximum (VBM). They also found that at the concentration of 6.25%, Na_{Cu} has stronger effect on the hole density of CIS than those of 8.33% and 12.5% incorporation of Na atoms. The present works are motivated by this theoretical study.

Despite of extensive experimental and theoretical studies of CIGS at ambient condition, none of them take high pressure effect into account. The high pressure effect is of major interests for the present research because in the CIS compound under high pressure, the band gap is getting wider in the chalcopyrite phase. Furthermore, the CIS exhibits a series of phase transitions from chalcopyrite $\rightarrow$ NaCl-like cubic structure $\rightarrow$ orthorhombic *Cmcm* structures [3]. In this work, the CIGS compound was investigated under high pressure, and it was firstly assumed that this material shares a similar transitions sequence with CIS. In order to incorporate the effects of Na atoms, the approximations of incorporation used two techniques which are the supercell and the mixture atoms methods. We focused on the replacement of Na on the Cu site, denoted by Na_{cu}, and on the In/Ga sites denoted by Na_{InGa}. The

effects on structural phase transitions and the electrical properties such as the electronic band gap and the electronic density of states (EDOS) were also fully investigated using *ab initio* calculations.

4.1 Calculation details

The simulation of Na effects was also performed by CASTEP code. The exchange-correlation function was the generalized-gradient approximation (GGA) functional of Perdew-Burke-Ernzerhof (PBE). The ultrasoft pseudopotential (the details shown in Figure 3.1) was used to represent the atoms in CIGS and Na. The pseudopotentials were composed of the potential from nuclei and some inner core electrons. The electronic structure solutions are governed by a number of valence electrons, i.e. 10 valence electrons of Cu, 13 valence electrons of In, 13 valence electrons of Ga, 6 valence electrons of Se, and 7 valence electrons of Na. From the optimization procedure of the CIGS primitive cell, the total energy starts to converge at 350 eV.
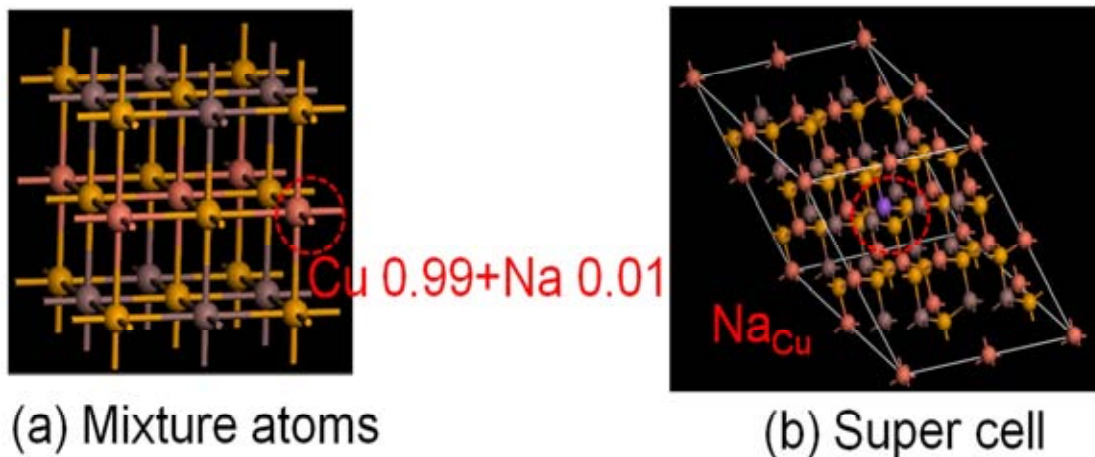
Figure 4.1: The type of Na-impurity methods (a) All Cu sites were mixed by Cu 99% and Na 1%. (b) a Na atom was replaced on a Cu site in super cell (Na_{Cu}).

The higher cutoff, i.e. 500 eV, gives a little more accuracy within the range of 6 meV/atom. Therefore, the energy cutoff was chosen at 350 eV for geometry

optimizations and at 500 eV for more accurate single point energy calculation. The energy tolerance in single point energy calculation was set at 0.01 meV/atom. The optimum k-point in Monkhorst-Pack grid size was found at 5×5×6 for chalcopyrite phase, and 5×5×5 for cubic and orthorhombic phases. For the Na substitutes, the 2 methods were imposed, as follows; the first method is called the mixture atom method, where we used the virtual crystal approximation (VCA) [62] to construct mixed atoms between Cu and Na, In and Na, and Ga and Na, shown in Figure 4.1. The similar method was successfully applied to study disorder in Pb(ZrTi)O_3 [62] and BiScO$_3$-PbTiO$_3$ [63]. The main idea of VCA is that the potential of the main atomic species (Cu, In or Ga) can be weakly perturbed by directly adding a small magnitude of the potential of the impurity (Na). For example, the potential of 1.0% Na on the Cu sites (denoted by 1.0% Na$_{Cu}$) is the summation of 0.99 times Cu potential and 0.01 times Na potential. To the lowest order, the physical properties of one 1.0% Na$_{Cu}$ atom is equivalent to the average over all configurations of the system of 99 Cu atoms and 1 Na atom. In the other words, the mixture potential represents the physical properties of a system of Cu majority with small amount of randomly distributed Na substitutes. The mixture potential, $V_{12}(\mathbf{r})$, can be written in terms of $V_1(\mathbf{r})$ and $V_2(\mathbf{r})$ as

$$V_{12}(\mathbf{r}) = w_1 V_1(\mathbf{r}) + w_2 V_2(\mathbf{r}), \tag{4.1}$$

where w_1 and w_2 are the percent by atom of mixed atoms respectively. By using mixture atom, we can calculate with low content (0.1%, 1.0% and 6.25%) of Na substitutes in CIGS and we can avoid counting large number of different random configurations. For the case of Na substituting on In and Ga sites, we scope ourselves to a special case where both sites were treated equally in terms of Na substitute. For example, 1.0% Na$_{InGa}$ means that there is 1.0% of Na on both In and Ga sites. We chose this special case because we wanted to compare the same composition as in the case of Na$_{Cu}$, and again to avoid counting large number of different configurations. The second method is called the supercell method, where we used a supercell of CIGS of size 2×2×2 unit cells. This supercell contains 16 Cu atomic basis. Then we replaced one of 16 Cu atomic basis by one Na so that the system contains 6.25% of

Na, shown in Figure 4.1(b). This can be used for comparing and verifying the results of mixture atom at 6.25% Na_{Cu} from the first method. In the supercell calculations, the geometries optimization was performed by using the energy cutoff at 300 eV and 2×2×2 k-points, while the single point energy and EDOS calculations were performed by using the energy cutoff at 350 eV. For finding structural phase transitions, it was considered the same as CIS by fitting the third order Birch-Murnaghan equation of state [64]. We estimated the band gap from the EDOS calculation. However, the GGA band gap is known to be underestimated. Instead, we chose to report only the trend of the band gap under pressure as it is in fair agreement with the experimental result [5, 8].
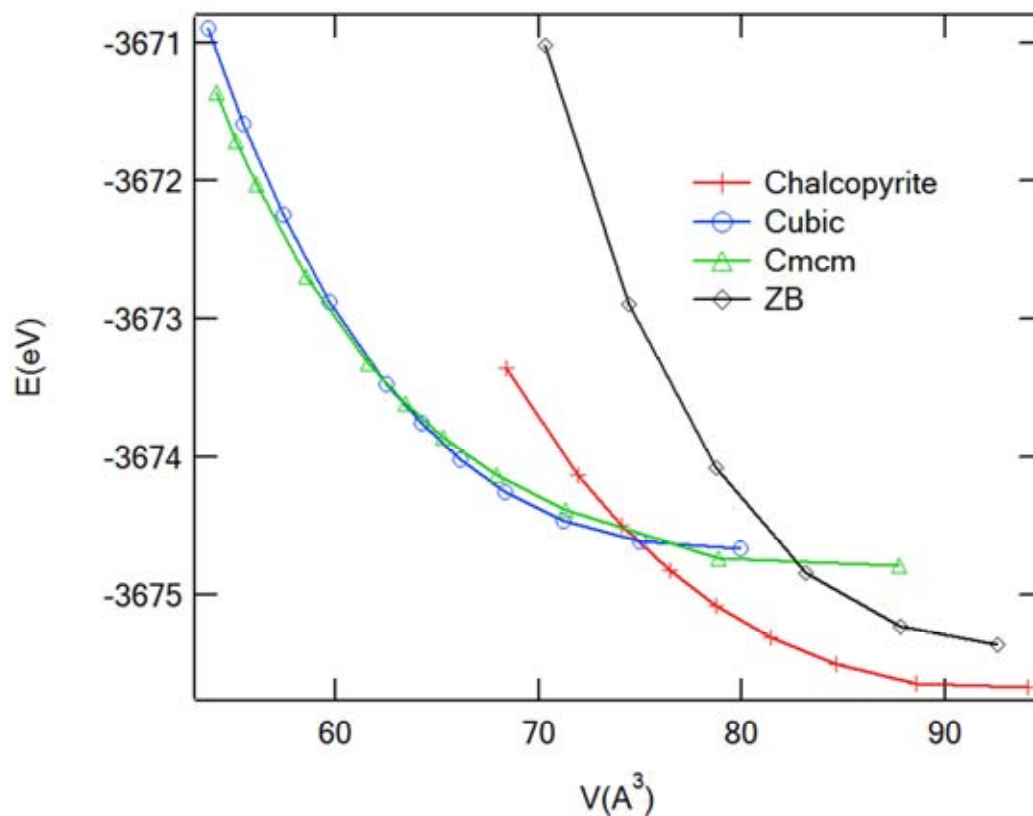
Figure 4.2: The E-V curves of pure CIGS show that the possible stable phases are chalcopyrite($I\bar{4}2d$), cubic($Fm\bar{3}m$) and *Cmcm* phases, while the trend of E-V points in zinc blende (ZB) show that it is unstable phase.
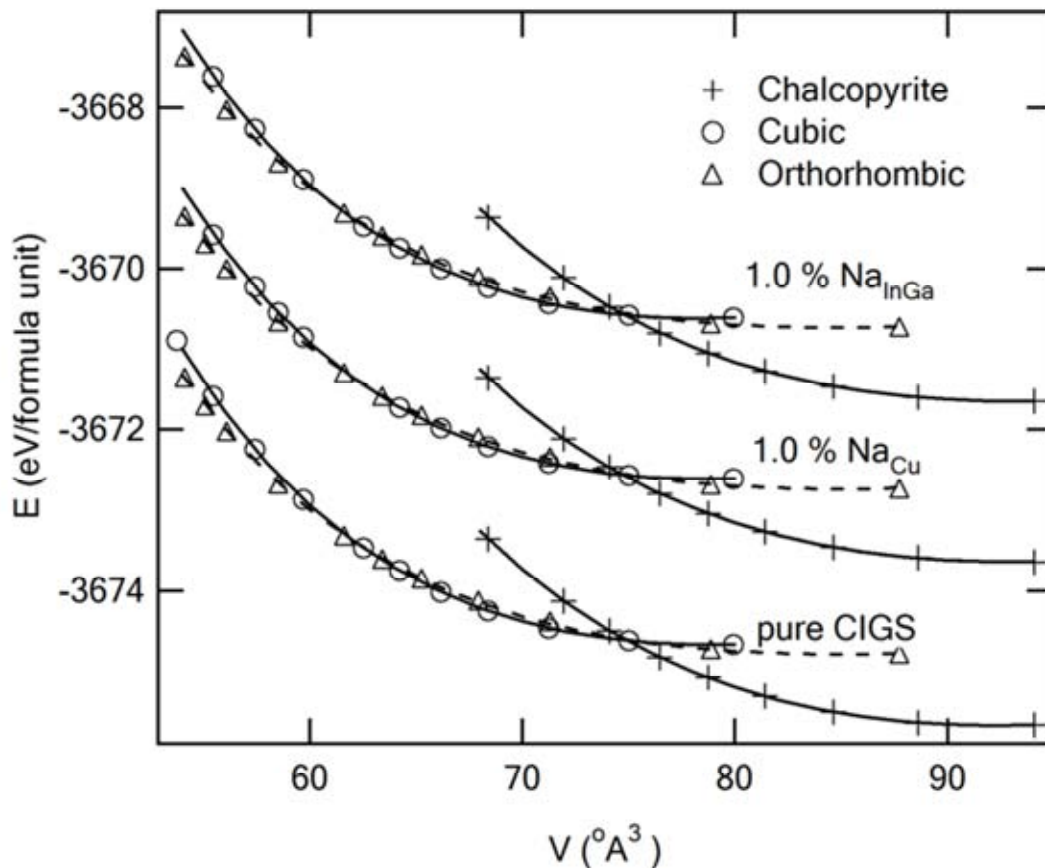
Figure 4.3: The E-V curves of pure CIGS, 1.0% Na_{Cu} and 1.0% Na_{InGa}. The high pressure phases were taken to be the same as CIS [3].

4.2 High pressure phases of doped CIGS

In order to investigate the high pressure phases of CIGS, we proposed that CIGS has the same series of phase transitions as of the CIS, which is chalcopyrite $\rightarrow$ NaCl-like $Fm\overline{3}m \rightarrow Cmcm$ structures [3]. The reason is that CIGS and CIS belong to the same group of the I-III-VI$_2$ compounds which have similar bondings and the similar structure at ambient condition. We also observed another phase. For example, we tested on the zinc blende (ZB) structure, which is closely related to the chalcopyrite phase and widely stable in binary compounds. The E-V curves in Figure 4.2 show that the possible stable phases of CIGS under high pressure are $I\overline{4}2d$, $Fm\overline{3}m$ and $Cmcm$ structures, while the ZB structure is an unstable phase simply because E-V curve of ZB gives the higher enthalpy in all high-pressure regions, the

details shown in Figure 2.4. Figure 4.3 showed the E-V curves of pure CIGS, 1.0% Na_{Cu} and 1.0% Na_{InGa}. By substituting 1.0% Na, the total energy of the system increased in all phases. At 0 GPa, the increasing energy per a formula unit from pure CIGS energy (E_{pure}) are $\Delta E_{1, 0\ GPa} = E_{Cu} - E_{pure} = 2.02$ eV, and $\Delta E_{2, 0\ GPa} = E_{In,Ga} - E_{pure}$ = 4.02 eV, where E_{Cu} and $E_{In,Ga}$ are total energy per a formula unit of the system with Na_{Cu} and Na_{InGa} respectively. The increasing energy at 50 GPa are $\Delta E_{1, 50\ GPa} = 1.69$ eV and $\Delta E_{2, 50\ GPa} = 3.67$ eV. Hence, the positive mixing enthalpy of Na_{Cu} is lower than that of Na_{InGa}. From Figure 4.3, the EOS of CIGS with different contents of Na exhibits slightly different slope. The slope of the EOS is related to the bulk modulus. Large modulus leads to low compressibility. In the other words, the material with large modulus is hard to be compressed. This term indicates the hardness of the material. From the EOS, we found that the hardness of CIGS is slightly reduced when Na substitutes are added. As a result, the enthalpy of CIGS with Na substitutes increases a little slower than that of pure CIGS. This result indicates that the Na substitutes can be easier added into CIGS at high pressure than at ambient pressure. We found that Na_{InGa} has larger effect on the energy than Na_{Cu} because the atomic size and the number of the valence electrons of Na differ from both In and Ga more than from Cu. This result confirmed that Na substituted on the Cu site is energetically preferable, as reported in previous studies [18, 19]. We analyzed the concentration of Na at 0.1% and found that the positive mixing enthalpy of 0.1% Na_{Cu} is 0.24 eV. The estimated deviation is about 0.05 eV. However, there is no significant effect on the transition pressure at small content of Na, i.e. 0.1% and 1.0% Na.

Next, we calculated the enthalpy of the system by using $H = E + PV$. For static calculation (T = 0 K), the enthalpy difference (H-H_0) was reported in pressure range of 0-50 GPa. The example of the enthalpy difference was shown in Figure 4.4. The pure CIGS has the phase transitions from $I\bar{4}2d$ to $Fm\bar{3}m$ at 13 GPa, and the volume reduction is 14.2 %. The phase transition from $Fm\bar{3}m$ to $Cmcm$ occurs at 24 GPa, and the volume reduction is 2.2 %. The estimated error bar of the EOS is about 1 GPa. Therefore, we concluded that 1.0% Na has no significant effect on the transition pressure and the volume reduction, whereas 6.25% Na produces noticeable effects on the transition pressure and the volume reduction, as shown in Table 4.1.
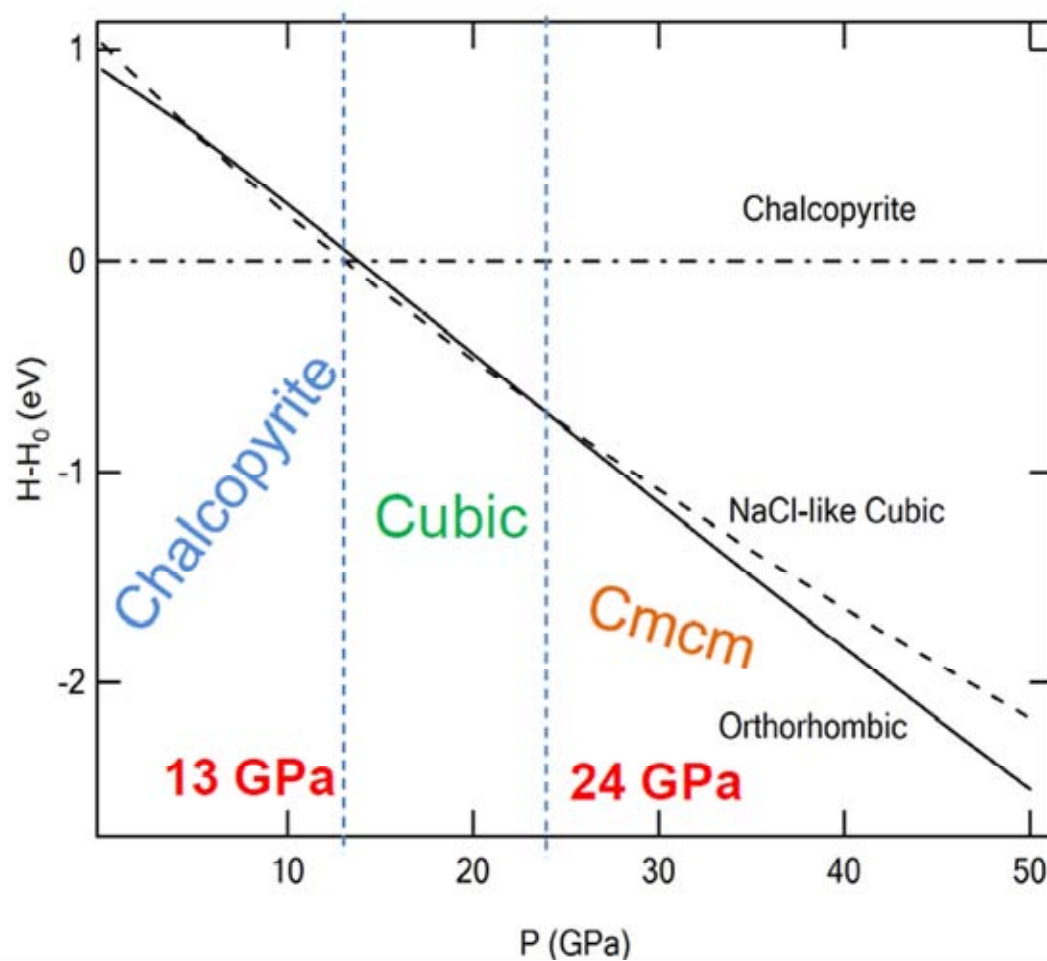
Figure 4.4: The example of the enthalpy difference (H-H_0) as a function of pressure of the system with 1.0% Na_{Cu}. The enthalpy of the chalcopyrite phase (H_0) was used as reference.

We also noticed that the *Cmcm* structure in the CIGS is different from the *Cmcm* in the binary compounds [65], due to the anti-symmetry of the 4 atoms in the CIGS unit cell. To clarify this difference, we set the atomic positions of Cu and Se(I) in the *Cmcm* CIGS unit cell to be the same as of the *Cmcm* in the binary compound. We found that the relative difference of the atomic positions at 25 GPa are Ga (-0.0083, -0.0167, 0.0046), In (0.0000, -0.0412, 0.0045), and Se(II) (0.0005, 0.0399, 0.0059). At this pressure, the atomic positions in *Cmcm* CIGS differ from the *Cmcm* of the binary compound by 4%, and it becomes close to the *Cmcm* binary compound when pressure increases, or volume of cell reduces.

Table 4.1: The transition pressure and volume reduction (-ΔV %) of the $I\bar{4}2d \rightarrow$ $Fm\bar{3}m \rightarrow Cmcm$ phase transitions.

Percent of Na in CIGS	Structural Phase Transition Transition Pressure (GPa) and Volume reduction (-ΔV%)	
	$I\bar{4}2d \rightarrow Fm\bar{3}m$	$Fm\bar{3}m \rightarrow Cmcm$
Pure CIGS	13 GPa (-14.2%)	24 GPa (-2.2%)
1.0% Na_{Cu}	13 GPa (-14.0%)	24 GPa (-2.2%)
1.0% Na_{InGa}	13 GPa (-14.2%)	25 GPa (-2.3%)
6.25% Na_{Cu}	14 GPa (-13.6%)	19 GPa (-1.6%)
6.25% Na_{InGa}	14 GPa (-14.0%)	18 GPa (-2.0%)

For 6.25% Na, we compared between the mixture atoms method and supercell method. We found that the transition pressure of the $Fm\bar{3}m$ to $Cmcm$ phase transition was reduced about 5-6 GPa as shown in Table 4.2. We verified the results from the mixture atoms method with the results from the supercell method, as shown in Figure 4.5. The enthalpy is slightly different between the two methods but it confirmed the transition pressure of the $Fm\bar{3}m$ to $Cmcm$ phase transition. We also found that 0.1% and 1.0% Na have no significant effect on the phase transition pressure. It is worth noticing here that the volume reduction due to the distortion ($Fm\bar{3}m$ to $Cmcm$) phase trasition is small, i.e. a few percent, whereas it was large in the reconstruction ($I\bar{4}2d$ $\rightarrow Fm\bar{3}m$) phase transition.

Table 4.2: The transition pressure and volume reduction of the $Fm\overline{3}m$ to $Cmcm$ phase transition.

Percent of Na on CIGS	Structural Phase Transition $Fm\overline{3}m \rightarrow Cmcm$	
	Pressure	Volume Reduction
Pure CIGS	24 GPa	-2.2 %
6.25 % Na_{Cu} (Mixture Atoms)	19 GPa	-1.6 %
6.25 % Na_{Cu} (Super Cell)	20 GPa	-2.0 %
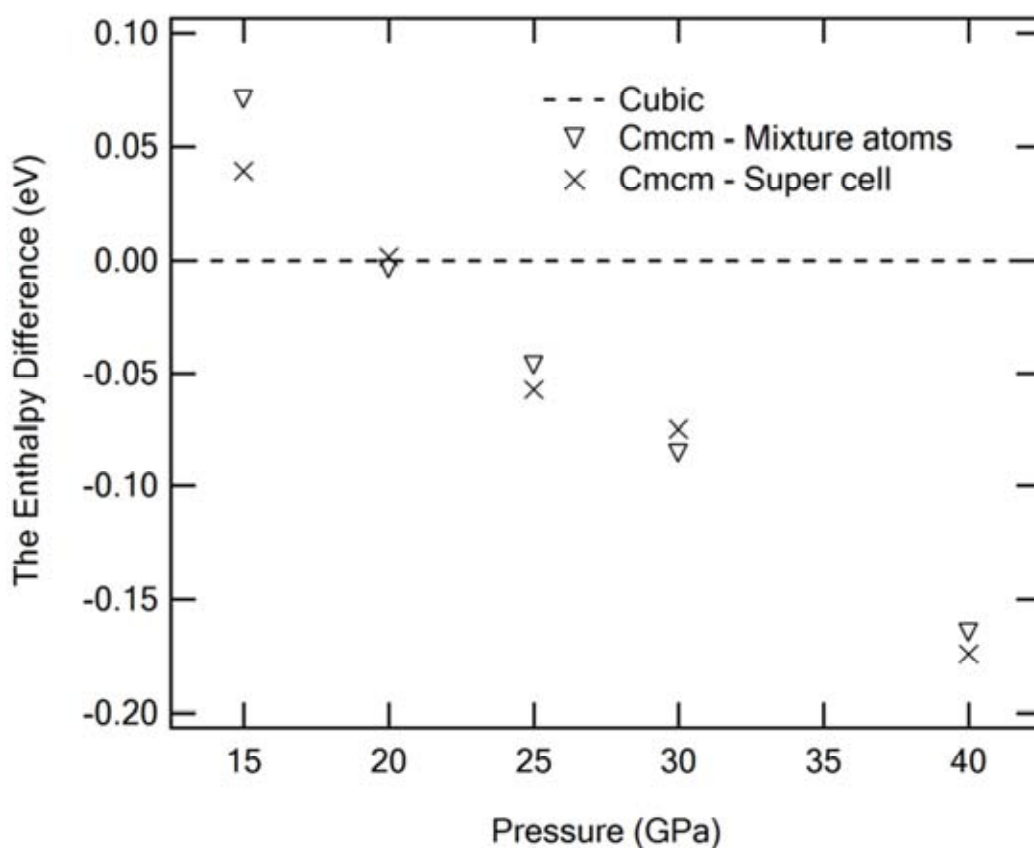
Figure 4.5: The H-P curves of the CIGS with 6.25% Na, near the $Fm\overline{3}m$ to $Cmcm$ phase transitions. The data points showed the comparison between the mixture atoms and supercell methods.

The large volume reduction at the $I\bar{4}2d$ to $Fm\bar{3}m$ transition occurs because it is a reconstruction phase transition, i.e. the Cu and (In,Ga) are coordinated by four neighbor Se atoms in the $I\bar{4}2d$ structure whereas they are coordinated by six neighbor Se atoms in the $Fm\bar{3}m$. On the other hand, the small volume reduction observed at $Fm\bar{3}m$ to $Cmcm$ transformation can be explained by the distortion of primitive cell. The $Fm\bar{3}m$ structure becomes denser than the $I\bar{4}2d$, as manifest itself in the volume reduction.

4.3 Effects of Na on hole density and band structure

At this stage, we analyzed the trends of the EDOS and the electronic band gap under pressure of the system with 6.25% Na_{Cu}. We found that the band gap only occurs in the chalcopyrite phase. In the cubic and orthorhombic phases, the gap is closed. The EDOS of the systems with 0.1% and 1.0% Na have no significant change from the pure CIGS. However, we found that the density of states near the valence band maximum (VBM) of the CIGS with 6.25% Na_{Cu} is higher than that of the pure CIGS at 5 GPa, see Figure 4.6 (a). In the semiconducting phase, the hole density or hole carrier concentration can be calculated from the integration of the product between the Fermi-Dirac distribution function and the EDOS near VBM. Therefore, the increasing EDOS near VBM will affect the hole density of CIGS. From Figure 4.6 (a), the EDOS of pure CIGS is increased by adding 6.25% Na_{Cu}, while Na_{InGa} reduced the peak of EDOS as valence band. From these results, we proposed that the Na is unlikely to substitute on In and Ga sites simply because size of Ga or In atom is significantly higher than Na atom, when compare to size of Cu atom. Moreover, the positive mixing energy of Na_{InGa} is also higher than Na_{Cu}. We also found that the EDOS near VBM decreases as pressure increases, as shown in Figure 4.6 (b). Figure 4.6 (b) also compared the results from the mixture atoms and the supercell methods. The results between the two methods have general agreement in that the 6.25% Na has an effect on the increasing of the EDOS, and the EDOS decreases as pressure increases.
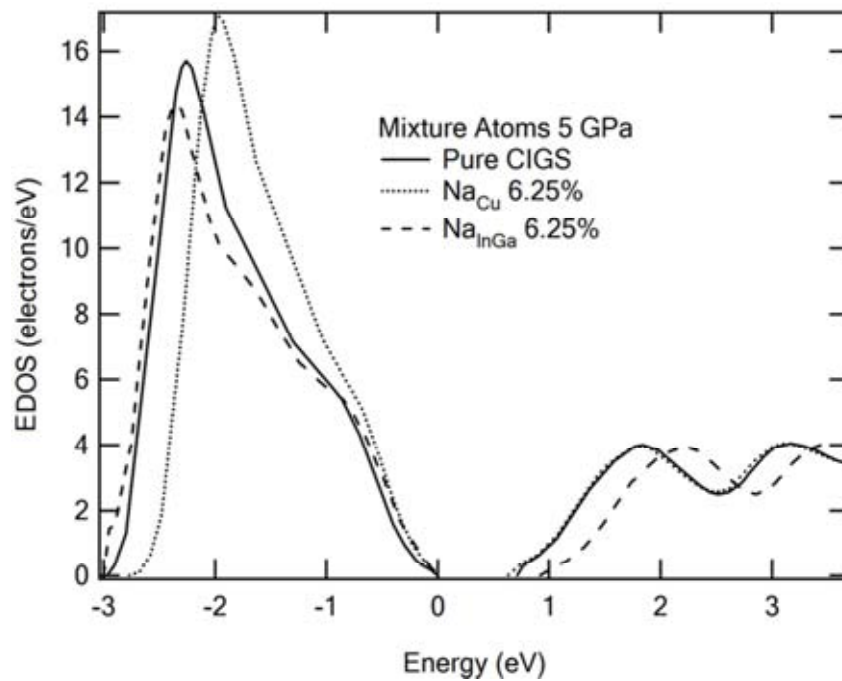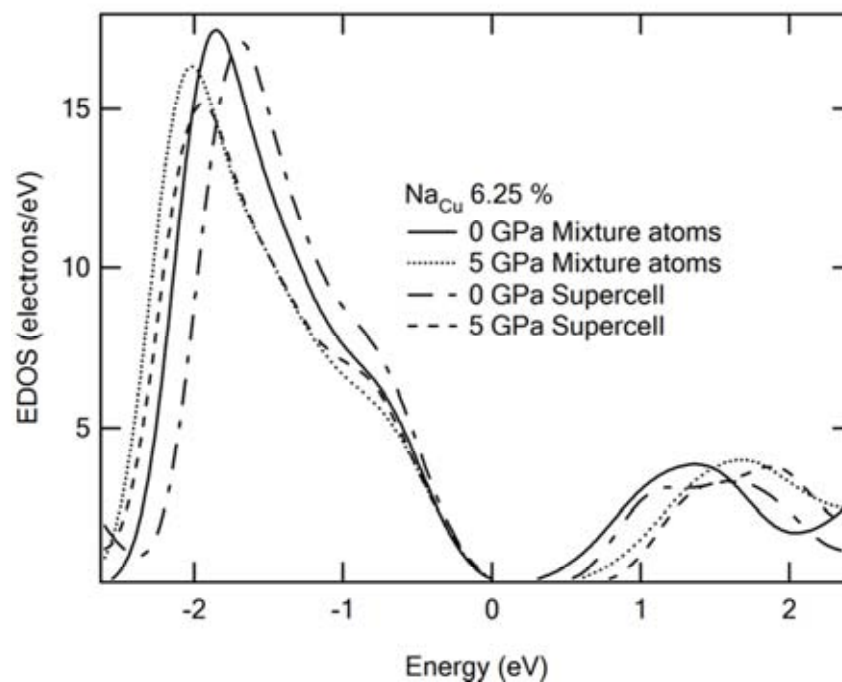
Figure 4.6: The EDOS near the VBM. (a) The comparison between the pure CIGS and the CIGS with 6.25% Na_{Cu}, and 6.25% Na_{InGa} at 5 GPa, using the mixture atoms method. (b) The trend of the EDOS near VBM at 0 and 5 GPa. The results were from the super cell and mixture atoms methods.

Table 4.3: The average bond length (Å) of the closest Cu-Se, In-Se and Ga-Se pairs in the $I\bar{4}2d$ phase at 0, 5 and 10 GPa, and the $Fm\bar{3}m$ phase at 15 GPa and the $Cmcm$ phase at 25 GPa. The stars (*) showed the average bond length of the system with 6.25% Na_{Cu}.

| Bond length | P (GPa) | | | | |
| | $I\bar{4}2d$ | | | $Fm\bar{3}m$ | $Cmcm$ |
(Å)	0	5	10	15	25
Cu-Se	2.43	2.36	2.31	2.58	2.57
In-Se	2.62	2.58	2.53	2.58	2.57
Ga-Se	2.45	2.41	2.37	2.57	2.51
Na_{Cu}-Se*	2.38	2.33	2.28	2.58	2.46
In-Se*	2.63	2.58	2.54	2.58	2.55
Ga-Se*	2.49	2.41	2.38	2.54	2.47

In addition, we can estimate the trend of the band gap under pressure from the EDOS. It was reported in the previous works that the energy gap increases with pressure in the $I\bar{4}2d$ phase [4]. We found that the band gap increases with the rate of 31 meV/GPa (mixture atoms) and 39 meV/GPa (super cell). These are in good agreement with the experimental result of Choi *et al.* [5]. Moreover, we found that the gap vanishes in the $Fm\bar{3}m$ and $Cmcm$ phases. The energy gap in the $I\bar{4}2d$ phase increases because the Cu-Se and (In,Ga)-Se bonds lengths are shortened under high pressure. The gap closure in the $Fm\bar{3}m$ and $Cmcm$ structures needs more sophisticated explanation. This could be because the local coordinations have changed from four Se atoms in the $I\bar{4}2d$ structure to six Se atoms in the $Fm\bar{3}m$ and $Cmcm$ structures. Although the size of primitive cell always reduces under pressure (Figure 4.3), the bond lengths substantially increase during the $I\bar{4}2d$ to $Fm\bar{3}m$ reconstruction phase transition, as shown in Table 4.3. For example, Cu-Se bond length at 0 GPa (2.43 Å) is shorter than the bond length at 15 GPa (2.58 Å) and 25 GPa (2.57 Å). The different bondings and bond lengths lead to more of the metal character. In CIGS, the bond lengths are increased due to phase transition; as a result, the band gap reduced or vanished. This result related with the trend of HOMO-LUMO

gap of CIS (Figure 3.15 and Table 3.6). It is worth noting also that even though the bond lengths in the $Fm\overline{3}m$ phase increase, but the overall volume is reduced by 14.0% as reported earlier.

CHAPTER V
Conclusions

In conclusions, we have used *ab initio* method to calculate the high pressure phases of CIS. It was found that CIS transform from the $I\bar{4}2d$ structure to the $Fm\bar{3}m$ structure at 12 GPa and then into the *Cmcm* structure at 42 GPa. The volume reductions at the phase transitions are 13.9% and 1.9% respectively. The sX-LDA band gap in the $I\bar{4}2d$ structure increases at the rate of 39.6 meV/GPa, in fair agreement with 30 meV/GPa from the previously reported photoabsorption experiment [4-5, 56]. The band gap is closed in the $Fm\bar{3}m$ and *Cmcm* structures. This indicates that, under high pressure, the semiconductor materials can transform their property to non-semiconductor materials along with their changed structures. The investigation on nature of bonding in the CIS under pressure has also been carried out and gave an explanation to the gap closure during the $I\bar{4}2d$ to $Fm\bar{3}m$ phase transition. The path of transformation from $Fm\bar{3}m$ to *Cmcm* was derived. The barrier between the two phases was estimated. The upper bound of the potential barrier is 17 meV. We can explain the co-exist phases found at room temperature experiment [3].

In the second articles, the *ab initio* calculation was used to investigate the effects of Na atoms on high pressure structural phase transitions of $CuIn_{0.5}Ga_{0.5}Se_2$. The high pressure phase transitions of CIGS to be the same has been reported to be similar sequence as of the CIS transitions sequence, i.e. $I\bar{4}2d \rightarrow Fm\bar{3}m \rightarrow Cmcm$ structures. The Na concentrations were chosen at 0.1, 1.0 and 6.25 %. The positive mixing enthalpy of Na_{InGa} is higher than Na_{Cu}. Thus Na substitutes on Cu sites are more energetically favorable than on Ga or In sites, in good agreement with previous studies [18, 19]. From the EOS under pressure, we found that the Na substitutes reduce the hardness (bulk modulus) of CIGS and they can be relatively easy to incorporate Na into CIGS under high pressure rather than at ambient pressure. The most significant effects occur at 6.25% Na. We found that the EDOS of CIGS near the VBM is increased noticeably in the chalcopyrite phase. This should lead to the

increase of the hole density. We found that the gap is close in the cubic and orthorhombic phases. Also, the Na_{Cu}-Se bond length in the chalcopyrite phase is significantly reduced at 6.25% Na, compared with pure Cu-Se bond length in the pure CIGS. This effect is correlated with the widening of energy band gap, and the gap increased at the rate of 31 meV/GPa under pressure. We also derived the path of transformation from the $Fm\bar{3}m$ to $Cmcm$ phase. The Cu-Se plane in the $Fm\bar{3}m$ phase displaced relatively parallel to the (In,Ga)-Se plane by 18% in order to transform to the $Cmcm$ phase. The enthalpy barrier is 0.020 eV/atom. From this finding, the coexist phases in room temperature experiments can be predicted.

From these studies, the novel information of the high-pressure structures and properties in ternary and quaternary compounds has been obtained. For the phase transition, most previous high pressure investigations were focus on elements and binary compounds because of their relatively simple space group symmetry. In this work, investigation on both structure phase transition and electronic phase transition has been extended to more complicate compounds (ternary and quaternary compounds). It is not trivial to get the stable high-pressure phase of a complex compound due to their nature of relatively low-symmetry. As a result, we have employed several possible space groups for the structure determinations. However, the stable phases of a complex compound can be obtained from the binary analog such as $I\bar{4}2d$ phase in CIS can also be viewed as a double c-axis structure of ZB. For Na doping, it was found that the changing pressure has significant effect on EDOS of CIGS more than the changing of impurity. The properties of the fabricating materials can also be changed by the external force. However, the Na impurity models in this work are assumed as the homogenous impurity incorporated into a solid which is not complete for predicting the experimental result. However, from this pioneer work, other complex materials maybe studied using the similar approach in order to disclose their potential application under extreme conditions.

References

[1]   J.E. Jaffe and A. Zunger. Theory of the band-gap anomaly in ABC_2
        chalcopyrite semiconductors. *Phys. Rev. B* 29 (1984): 1882.

[2]   T. Tinoco, A. Polian, D. Gomez, and J. P. Itie. Structural Studies of $CuInS_2$
        and $CuInSe_2$ under High Pressure. *Phys. Stat. Sol. (b)* 198 (1996): 433.

[3]   T. Bovornratanaraks, V. Saengsuwan, K. Yoodee, M. I. McMahon, C. Hejny,
        and D. Ruffolo. High pressure orthorhombic structure of $CuInSe_2$.
        J. Phys.: Condens. Matter 22 (2010): 355801.

[4]   J. Gonźalez and C. Rinćon. Optical absorption and phase transitions in
        $CuInSe_2$ and $CuInS_2$ single crystals at high pressure. *J. Appl. Phys.* 65
        (1991): 2031.

[5]   I. Choi and P. Y. Yu. Pressure Dependence of Band Gaps in the Quaternary
        Semiconductors Cu(In, Ga)Se_2. *Phys. Stat. Sol. (b)* 211 (1996): 143.

[6]   M. Belhadj, A. Tadjer, B.Abbar, Z. Bousahafs, and H. Aourag. Structural,
        electronic and optical calculations of Cu(In,Ga)Se_2 ternary
        chalcopyrites. *Phys. Stat. Sol. (b)* 241 (2004): 2516.

[7]   T.Maeda and T.Wada. Electronic Structure and Characteristics of Chemical
        Bonds in $CuInSe_2$, $CuGaSe_2$, and $CuAlSe_2$. *Japan J. Appl. Phys.* 49
        (2010): 04DP07.

[8]   J. Vidal, S. Botti, P. Olsson, J. Guillemoles, and L. Reining. Strong Interplay
        between Structure and Electronic Properties in CuIn(S,Se)$_2$: A First-
        Principles Study. *Phys. Rev. Lett.* 104 (2010): 056401.

[9]   D. Rudmann. *Effects of sodium on growth and properties of Cu(In,Ga)Se_2 thin
        films and solar cells*, PhD thesis University of Basel 2004.

[10]   D. Braunger, D. Hariskos, G. Bilger, U. Rau and H.W. Schock. Influence of
        sodium on the growth of polycrystalline $Cu(In,Ga)Se_2$ thin films. *Thin
        Solid Films* 361 (2000): 161.

[11]   K. Granath, M. Bodegard and L. Stolt. The effect of NaF on $Cu(In, Ga)Se_2$
        thin film solar cells *Sol. Energy Mater. Sol. Cells.* 60 (2000): 279.

[12]   Y.M. Shin, D.H. Shin, J.H. Kim and B.T. Ahn. Effect of Na doping using
        Na_2S on the structure and photovoltaic properties of CIGS solar cells.
        Current Appl. Phys. 11 (2011): S59.

[13]   M. Bodegard, K. Granath, and L. Stolt. Growth of $Cu(In,Ga)Se_2$ thin films by
        coevaporation using alkaline precursors. *Thin Solid Films* 9 (2000):
        361.

[14]   D.J. Schroeder. and A. Rockett. Electronic effects of sodium in epitaxial
        $CuIn_{1-x}Ga_xSe_2$. *J. Appl. Phys.* 82 (1997): 4982.

[15]   R. Sakdanuphab, C. Chityuttakan, A. Pankiew, N. Somwang, K. Yoodee and
        S. Chatraphorn. Growth characteristics of $Cu(In,Ga)Se_2$ thin films
        using 3-stage deposition process with a NaF precursor. *J. Cryst.
        Growth.* 319 (2011): 44.

[16]   R. Caballero, C.A. Kaufmann, T. Eisenbarth, M. Cancela, R. Hesse, T. Unold,
        A. Eicke, R. Klenk and H.W. Schock. The influence of Na on low
        temperature growth of CIGS thin film solar cells on polyimide
        substrates. *Thin Solid Films* 517 (2009): 2187.

[17]   Y.J. Zhao and A. Zunger. Site preference for Mn substitution in spintronic
        $CuM^{III}X_2^{VI}$ chalcopyrite semiconductors. *Phys. Rev. B* 69 (2004):
        75208.

[18]   S. Wei, S.B. Zhang and A. Zunger. Effects of Na on the electrical and structural properties of CuInSe$_2$. *J. Appl. Phys.* 85 (1999): 7214.

[19]   Z.B. Li, X. Wang and K.L. Yao. Electronic structures and optical properties of Cu$_{1-x}$Na$_x$InSe$_2$ by first-principle calculations. *Solid State Commun.* 150 (2010): 1514.

[20]   M. Born and R. Oppenheimer. On the Quantum Theory of Molecules. *Ann. Phys.* 84 (20) (1927): 457.

[21]   A. Szabo, N.S. Ostlund. Modern Quantum Chemistry. Mineola, New York. 1996.

[22]   A. Hinchliffe. *Modeling Molecular Structures* (2nd ed.). Baffins Lane, Chichester, West Sussex PO19 1UD, England: John Wiley & Sons Ltd. (2000): 186.

[23]   Hohenberg and W. Kohn. Inhomogeneous electron gas. *Phys. Rev.* 136 (3B) (1964): B864.

[24]   T. Rowland. *Functional,* Math World.

[25]   R.G. Parr and W. Yang. *Density functional theory of atom and molecules*, 1989.

[26]   Tomas Arias. *Kohn-Sham equations*, 2004.

[27]   W. Kohn and L.J. Sham. Self-consistent equations including exchange and correlation effects. *Phys. Rev.* 140 (4A) (1965): A1133.

[28]   Parr, G. Robert, Yang and Weitao. *Density-Functional Theory of Atoms and Molecules*, 1994.

[29]   J.P. Perdew and A. Zunger. Self-interaction correction to density-functional approximations for many-electron systems. *Phys. Rev. B* 23 (10) (1981): 5048.

[30] Parr, Robert G; Yang, Weitao. *Density-Functional Theory of Atoms and Molecules*. Oxford: Oxford University Press, 1994.

[31] D.C. Langreth and J.P. Perdew. Theory of nonuniform electronic systems. I. Analysis of the gradient approximation and a generalization that works. *Phys. Rev. B* 21(1980): 5469.

[32] J.P. Perdew and Y. Wang. Accurate and simple density functional for the electronic exchange energy: Generalized gradient approximation**.** *Phys. Rev. B* 33 (1986): 8800.

[33] F. Gygi and A. Baldereschi. Self-consistent Hartree-Fock and screened-exchange calculations in solids: Application to silicon. *Phys. Rev. B* 34 (1986): 4405.

[34] A. Seidl, A. Görling, P. Vogl, J.A. Majewski, and M. Levy. Generalized Kohn-Sham schemes and the band-gap problem**.** *Phys. Rev. B* 53 (1996): 3764.

[35] J. Lento. Master's thesis, Helsinki University of Technology, 1997.

[36] S. Chawla and A.G. Voth. Exact exchange in ab initio molecular dynamics: An efficient plane-wave based algorithm. *J. Chem. Phys.* 108 (1998): 4697.

[37] J.M. Soler, E. Artacho, J.D. Gale, A. Garcia, J. Junquera, P. Ordejon and D. Sanchez-Portal. The SIESTA method for *ab initio* order-*N* materials simulation. *J. Phys.: Condens. Matter* 14 (2002): 2745.

[38] D. R. Bowler, T. Miyazaki and M. J. Gillan. Recent progress in linear scaling *ab initio* electronic structure techniques. *J. Phys.: Condens. Matter* 14 (2002): 2781.

[39] S. Goedecker. Linear scaling electronic structure methods. *Rev. Mod. Phys.* 71 (1999): 1085.

[40] C. Kittel. *Introduction to Solid State Physics*. New York: Wiley, 1996.

[41] N.W. Ashcroft and N.D. Mermin. *Solid State Physics.* Orlando: Harcourt, 1976.

[42] M.C. Payne, M.P. Teter, D.C. Allan, T.A. Arias, and D. Joannopoulos. Iterative minimization techniques for *ab initio* total-energy calculations: molecular dynamics and conjugate gradients**.** *Rev. Mod. Phys.* 64 (1992): 1045.

[43] H.J. Monkhorst and J.D. Pack. Special points for Brillouin-zone integrations. *Phys. Rev. B* 13 (1976): 5188.

[44] R.P. Feynman. Forces in Molecules. *Phys. Rev.* 56 (4) (1939): 340.

[45] J.S. Toll. Causality and the Dispersion Relation: Logical Foundations. *Physical Review* 104 (1956): 1760.

[46] F.D. Murnaghan. The Compressibility of Media under Extreme Pressures *Proceedings of the National Academy of Sciences of the United States of America* 30 (9) (1944): 244–247.

[47] F. Birch. Finite Elastic Strain of Cubic Crystals. *Phys. Rev.* 71 (1947): 809.

[48] L.D. Landau and E.M. Lifshitz. *Statistical Physics Part 1*, vol. 5 of Course of Theoretical Physics, Pergamon, 3rd Ed. 1994.

[49] J.M. Yeomans. *Statistical Mechanics of Phase Transitions* Oxford University Press, 1992.

[50] T. Li, H. Luo, R.G. Greene, A.L. Ruoff, S.S. Trail and F.J. DiSalvo. High Pressure Phase of MgTe: Stable Structure at STP. *Phys. Rev. Lett.* 74 (1995): 5232.

[51] M.D. Segall, P.L.D. Lindan, M.J. Probert, C.J. Pickard, P.J. Hasnip, S.J. Clark, and M.C. Payne. First-principles simulation: ideas, illustrations and the CASTEP code. *J. Phys.: Cond. Matt.* 14 (2002): 2717.

[52] J.P. Perdew, J.A. Chevary, S.H. Vosko, K.A. Jackson, M.R. Pederson, D.J. Singh, and C. Fiolhais. Atoms, molecules, solids, and surfaces: Applications of the generalized gradient approximation for exchange and correlation *Phys. Rev. B* 46 (1992): 6671.

[53] J.P. Perdew, K. Burke and M. Ernzerhof. Generalized Gradient Approximation Made Simple. *Phys. Rev. Lett.* 77 (1996): 3865.

[54] J. Parkets, R.D. Tomlinson, and J. Hampshire. Crystal data for $CuInSe_2$. *J. Appl. Cryst.* 6 (1973): 414.

[55] H. Neumann. Bulk Modulus-Volume Relationship in Ternary Chalcopyrite Compounds. *Phys. Stat. Solid. (a)* 96 (1986): K121.

[56] S. Wei, A. Zunger, I.H. Choi, and P.Y. Yu. Trends in band-gap pressure coefficients in chalcopyrite semiconductors. *Phys. Rev. B* 58 (1998): R1710.

[57] H.W. Spiess, V. Haeberln, G. Brandt, A. Räuber, and J. Schneider. Nuclear Magnetic Resonance in IB–III–VI2 Semiconductors. *Phys. Stat. Solid. (b)* 62 (1974): 183.

[58] S.C. Abrahams and J.L. Bernstein. Piezoelectric Nonlinear Optic $CuGaSe_2$ and $CdGeAs_2$: Crystal Structure, Chalcopyrite Microhardness, and Sublattice Distortion. *Journal of Chemical Physics* 61 (1974): 1140.

[59] R. Asokamani, R.M. Amirthakumari, R. Rita, and C. Ravi. Electronic Structure Calculations and Physical Properties of ABX_2 (A = Cu, Ag; B = Ga, In; X = S, Se, Te) Ternary Chalcopyrite Systems. *Phys. Stat. Solid. (b)* 213 (1999): 349.

[60] T. Tinoco, J. P. Itié, A. Polian, A. San Miguel, E. Moya, P. Grima, J. Gonzalez and F. Gonzalez. Combined X-Ray Absorption and X-Ray Diffraction Studies of $CuGaS_2$, $CuGaSe_2$, $CuFeS_2$ and $CuFeSe_2$ under High Pressure. *Journal De Physique IV* 4 (1994): C9.

[61] S.B. Zhang, S. Wei, A. Zunger, H. Katayama-Yoshida. Defect physics of the $CuInSe_2$ chalcopyrite semiconductor. *Phys. Rev. B* 57 (1998): 9642.

[62]   L. Bellaiche and D. Vanderbilt. Virtual crystal approximation revisited:

Application to dielectric and piezoelectric properties of perovskites.

Phys. Rev. B 61 (2000): 7877.

[63]   J. Iniguez, D. Vanderbilt and L. Bellaiche. First-principles study of

$(BiScO_3)_{1-x}$-$(PbTiO_3)_x$ piezoelectric alloys. *Phys. Rev. B* 67 (2003):

224107.

[64]   A. Phusittrakool, T. Bovornratanaraks, R. Ahuja and U. Pinsook. High

pressure structural phase transitions in Sr from *ab initio* calculations.

Phys. Rev. B 77 (2008): 174118.

[65]   M. Durandurdu and D.A. Drabold. *Ab initio* simulation of high-pressure

phases of GaAs. *Phys. Rev. B* 66 (2002): 45209.

Appendix

CASTEP code

Cambridge Serial Total Energy Package or CASTEP is a commercial (and academic) software package which uses density functional theory with a plane wave basis set to calculate the electronic properties of crystalline solids, surfaces, molecules, liquids and amorphous materials from first principles. First principle calculations allow researchers to investigate the nature and origin of the electronic, optical, and structural properties of a system without the need for any experimental input. CASTEP is well suited to research problems in solid state physics, materials science, chemistry, and chemical engineering where empirical models are lacking and experimental data may be sparse. In these areas, researchers can employ computer simulations to perform virtual experiments, leading to tremendous savings in costly experiments and shorter developmental cycles.

CASTEP has been completely written for use on parallel computers by researchers at the Universities of York, Durham, St. Andrews, Cambridge and Rutherford Labs. The code is developed by the Castep Developers Group (CDG) who are all UK based academics. Current CDG members are:

Matthew Segall - Main author of the code specification, responsible for all the low-level communications and basis set coding, and the population analysis algorithms.

Matt Probert - Responsible for the geometry optimization and molecular dynamics coding, and keeper of the parameters module.

Stewart Clark - Responsible for the band structure, exchange-correlation functional coding and keeper of the cell module, and co-author of the linear response code.

Chris Pickard - Responsible all pseudopotential coding, and co-author of the NMR code.

Phil Hasnip - Responsible for the electronic minimization coding, including density mixing and ensemble DFT.

Keith Refson - Responsible for phonon and E-field calculations and co-author of the linear response code.

Jonathan Yates - Co-author of the NMR and related spectoscopies code.

Mike Payne - CASTEP creator and general overseer of the whole project.

Starting from the many-body wavefunction, an adiabatic approximation is made with respect to the nuclear and electronic coordinates (the Born-Oppenheimer approximation). The code also makes use of Bloch's Theorem which means a wavefunction of a periodic system has a cell-periodic factor and a phase factor. The phase factor is represented by a plane wave. From the usage of Bloch's Theorem, it is ideal to write the wavefunction in plane waves for the cell-periodic factor and the phase factor. From this the basis functions are orthogonal and it is easy to perform a Fourier transform from real to reciprocal space and vice versa. Fast Fourier Transforms are used throughout the CASTEP code, as is the Ewald summation method for Coulombic energies. Along with plane waves and conjugate gradient minimization, pseudopotentials are essential to the CASTEP code for reducing the computational expense of the calculation. Pseudopotentials replace the atomic nucleus and the core electrons by an effective numeric potential.

CASTEP permits geometry optimization and finite temperature molecular dynamics with implicit symmetry and geometry constraints, as well as calculation of a wide variety of derived properties of the electronic configuration. CASTEP can simulate a wide range of properties of materials proprieties including energetics, structure at the atomic level, vibrational properties, electronic response properties etc. In particular it has a wide range of spectroscopic features that link directly to experiment, such as infra-red and Raman spectroscopies, NMR, and core level spectra. CASTEP can be used to calculate the full tensor of second-order elastic constants and related mechanical properties of a crystal (Poisson coefficient, Lame constants, bulk modulus). The transition-state searching tools in CASTEP enable you to study chemical reactions in either the gas phase or on the surface of a material using linear synchronous transit/quadratic synchronous transit technology. These tools can also be used to investigate bulk and surface diffusion processes. Furthermore, the vibrational properties of solids (phonon dispersion, total and projected density of phonon states, thermodynamic properties) can be calculated with CASTEP using either the linear response methodology or the finite displacements technique. The results can be used in various ways, for instance, to investigate the vibrational properties of adsorbates on surfaces, to interpret experimental neutron spectroscopy

data or vibrational spectra, to study phase stability at high temperatures and pressures, etc. The linear response method can also be used to calculate the response of a material to an applied electric field - polarizability for molecules and dielectric permittivity in solids - and to predict IR spectra. You can see the additional details of CASTEP in website www.castep.org.

International Publications:

1. <u>P. Pluengphon</u>, T. Bovornratanaraks, S. Vannarat, K. Yoodee, D. Ruffolo and U. Pinsook, "*Ab initio* calculation of high pressure phases and electronic properties of $CuInSe_2$" *Solid State Communications*, volume **152** (2012) page 775, impact factor 1.976.

2. <u>P. Pluengphon</u>, T. Bovornratanaraks, S. Vannarat and U. Pinsook, "The effects of Na on high pressure phases of $CuIn_{0.5}Ga_{0.5}Se_2$ from *ab initio* calculation" *Journal of Physics: Condensed Matter*, volume **24** (2012) page 095802, impact factor 2.332.

International Conference:

1. <u>P. Pluengphon</u>, T. Bovornratanaraks, S. Vannarat and U. Pinsook, "The effects of Na on high pressure phases of $CuIn_{0.5}Ga_{0.5}Se_2$ from *ab initio* calculation" oral presentation in *The 7th Mathematics and Physical Sciences Graduate Congress* 12-14 December 2011 in National University of Singapore.

National Conferences:

1. <u>P. Pluengphon</u>, T. Bovornratanaraks, S. Vannarat and U. Pinsook, "The First Structural Phase Transitions of $CuGaSe_2$ under High Pressure" oral presentation in *Siam Physics Congress 2011* (SPC2011) 23-26 March 2011 in Ambassador City Jomtien Hotel, Chonburi Thailand.

2. <u>P. Pluengphon</u>, T. Bovornratanaraks, S. Vannarat and U. Pinsook, "Structural Phase Transitions of $CuIn_xGa_{1-x}Se_2$ under High Pressure by *ab initio* Method" oral presentation in *Science and Technology Conference 2011* 15 March 2011 in Huachiew Chalermprakiet University Thailand.

Biography

Mr. Prayoonsak Pluenphon was born on 2 August 1981 in Chondaen district, Phetchaboon province, Thailand. In 1998, he got High School level from Dongkhui Wittayakhom School. And then, he received the Bachelor degree in Physics (B.Sc. Physics), Department of Physics and Material Science, Faculty of Science, Chiang Mai University, in 2003. The senior project in B.Sc. studied about ions implantation of Nitrogen, Cabon and Oxygen on the steel target. The advisor in B.Sc. is Assoc.Prof.Dr. Somsorn Singkharat. Afterwards, he studied the Master degree in Physics (M.Sc. Physics) in 2006. The topic in M.Sc. is "Dimension effect on electrical properties of semiconductor calculated from density of state". The advisor in M.Sc. is Asst.Prof.Dr. Supab Choopun. In 2008, he started to study this PhD program with their advisor Asst.Prof.Dr. Thiti Bovornratanaraks in the Extreme Condition Physics Research Laboratory, Department of Physics, Faculty of Science, Chulalongkorn University.